Uncertainties Introduced by the Ocean Surface when Conducting Airborne Lidar Bathymetry Surveys

Master Thesis

Torbjörn Karlsson

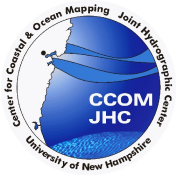

LUND INSTITUTE OF TECHNOLOGY
Lund University

December 13, 2011

English abstract

A method for investigating how the ocean surface affects the accuracy of Airborne Lidar Bathymetry surveys, (ALB), due to environmental conditions, was developed. Computer graphic techniques were examined and utilized for construction of realistic ocean surfaces. Wave spectrum models available in the literature describing the wave number composition of ocean surfaces were used in order to be able to change the environmental conditions. Realistic ocean surface conditions for conducing ALB surveys were narrowed down and ray tracing was performed on these surfaces using thousands of rays with setups similar to those conditions. The direction for each ray was stored before and after intersecting the air/water interface. Changes in the ray direction for different environmental conditions were studied by varying the input parameters of the wave spectrum model. Aspects that were examined include: whether there are any changes in the mean direction of the pulses, how much the mean direction of the pulses deviates from the average direction and how the footprint shape on the sea floor affects the probability of detecting targets. The result showed that wind speed, fetch size and diameter of the laser beam on the water surface all contribute to the overall accuracy of the pulse direction while the main direction of all pulses remains unchanged. The investigation technique was verified by conducting real experiments on a small scale setup while at the same time measuring the wave spectrum. Theoretical surfaces were generated, making use of the measured spectrum, and ray traced. The results were compared showing relatively good agreement between the consecutive ray tracing and the experiments.

Populärvetenskaplig sammanfattning

Luftburen lidarbatymetri är en teknik som används vid mätning av sjö- och havsbottnar för att skapa underlag till sjökort med mera. Tekniken bygger på att en laserpuls, utsänd från ett luftburet lidarsystem, träffar havsytan och den reflekterade signalen analyseras. I signalen återfinns två toppar. Den första uppstår då laserpulsen träffar vattenytan och delar av ljuset reflekteras tillbaka. Den andra toppen uppkommer av det ljus som reflekteras i botten. Genom att mäta tiden mellan de båda topparna kan man räkna ut skillnaden i ljusets färdväg. Därigenom kan man sedan bestämma vattendjupet.

Ljus som faller in mot en vattenyta ifrån luften bryts in mot ytans normal. Den nya riktningen bestäms med hjälp av Snells lag, även kallad refraktionslagen. När man utför batymetriska mätningar vet man vilken riktning ljuset har då det träffar vattenytan. Vad den refrakterade riktningen blir beror på utseendet hos vattenytan. När laserpulsen färdas framåt breddas den och har en diameter på flera meter då den når vattenytan. Det gör att laserljuset kommer att träffa ett stort antal vattenvågor och därmed brytas upp i olika riktningar. Följden blir att man inte säkert vet vilken den nya huvudsakliga utbredningsriktningen kommer att bli. Istället gör man approximationen att ytan är platt, vilket i sin tur kommer att leda till ett mätfel.

Det här projektet försöker kartlägga hur laserljusets riktningar påverkas utav vattenytan. För att lyckas med detta måste ytans beskaffenhet först bestämmas, vilket i sin tur beror på lokala förhållanden som vindhastighet. Undersökningen har gjorts genom att utveckla ett datorprogram som simulerar förloppet när en laserpuls träffar och sedan bryts i vattenytan.

Realistiska ytstrukturer har konstruerats i form av triangelnät. Strukturerna har skapats med utgångspunkt i spektrala modeller som beskriver hur havsytan definieras som en sammansättning av planvågor. Tillsammans skapar dessa planvågor en komplicerad struktur som ger en god beskrivning av vattenytan förutsatt att den spektrala sammansättningen är korrekt. Laserpulserna simulerades med hjälp av tusentals enskilda strålar. Var och en av dessa strålar träffar en facett i triangelnätet och bryts av i någon riktning. Dessa strålar kan sedan användas för att simulera en intensitetsprofil på botten eller användas för att beräkna pulsens medelutbredningsriktning.

Genom att simulera hur ett stort antal pulser träffar unika vågytor - skapade under likadana förutsättningar - kan en sannolikhetsfördelning över medelutbredningsriktningen erhållas. Denna kan användas vid beskrivning av osäkerheten som härör från vattenytan. Är man intresserad av sannolikheten att upptäcka ett mål på havsbottnen kan man i stället undersöka antalet strålar som träffar respektive missar målet beroende på ytförhållanden och djup.

Resultaten visar att ytförhållanden och laserfläckens storlek påverkar osäkerheten i mätningarna. Exempelvis påvisades en 50 procent större osäkerhet för en laserfläck med en diameter på 1,5 m jämfört med en motsvarande diameter på 4,5 m då vindhastigheten var 5 m/s.

För att kontrollera att simuleringsmetoden ger realistiska resultat har även småskaliga mätningar utförts i en vågbassäng. En laserstråle belyste en vågyta och formen på laserfläcken under vattnet dokumenterades med hjälp av en undervattenskamera. Samtidigt uppmättes vattenytans elevation. Genom att simuleringsmodellen efterliknade experimentet kunde en jämförelse göras mellan resultaten, vilket visade på god överensstämmelse.

Acknowledgements

The project has been very exciting and there are many persons who contributed to that and also helped me along the way. For that I am very grateful. I would like to give a big "thank you" to Dr. Shachak Pe'eri at the Center for Coastal and Ocean Mapping (CCOM) for the warm welcoming to the United States and the hospitality during my time at the facilities and for all the support along the entire project. This includes times both at work and outside. There are also several other persons at CCOM I would like to thank. Dr. Jame Irish for interesting discussions about waves and wave spectrum measurements, Dr. Thomas Lippmann for discussions about sea conditions and help with understanding the Fourier analysis and Yuri Rzhanov for the help with image recording and image analysis. I would also like to thank Dr. Lee Alexander and his family for all their support and hospitality.

My supervisor, Andreas Axelsson, at Airborne Hydrography AB also deserves a very big thank. First of all for giving me the opportunity to do this project but also for all the valuable help along the way. I would also like to thank my supervisor at Lund University, Gabriel Somesfalean, for the help of making my report scientific and keeping it up to the standards.

My deepest gratitude goes to my fiancée, Emmelie, for her support at all times and for her being patient with me spending a long time on the other side of the Atlantic and many late nights at the office. At last, my - at all times - supporting family should not go unnoticed and deserves my greatest appreciation for their support, today as well as through the years.

Contents

Chapter 1

Introduction

1.1 Background

Through the recent decades Airborne Lidar Bathymetry (ALB) has emerged as an effective technique for bathymetric surveys [2]. By mounting an ALB system into an aircraft, rapid bathymetric surveys can be conducted over near shore areas where traditional sonar methods are ineffective due to low coverage rate. The ALB method is effective for water depths up to two or three times the secchi depth.[1]

Lidar is a general method used in remote sensing systems in a variety of fields. It is an acronym based on the same principles as *radar* and *sonar* and stands for **Li**ght **D**etection **A**nd **R**anging. Short pulses of laser light are launched from the system and the reflected pulse is recorded and analysed. When using lidar for bathymetric surveys there are especially two peaks in the return signal that are of particular interest. The first one rises from the reflection when the laser pulse intersects the water surface causing some part of the light to return to the system. The second peak is a result from the reflection at the seafloor. By measuring the time difference and knowing the incident angle the water depth can be calculated.

Light intersecting the air/water interface changes its direction of propagation according to the laws of refraction. If the light is incident from air, which is optically thinner than water, the new direction will be adjusted towards the surface normal of where the intersection occurred.

In order to evaluate how the ALB laser beam changes due to different sea surface conditions one needs to understand how the facets at the air/water interface, illuminated by the laser footprint, introduce new directions of propagation of the laser light. An investigation of the ray path geometry is needed in order to evaluate the refraction of the ALB laser beam due to its interaction with different sea surface conditions. Accurate knowledge about the existing slopes of water facets and especially the slope distribution across the water surface, is vital for understanding the changes of the ALB laser beam.

In order to be able to study the changes of the laser light directions due to the water surface conditions those surface conditions need to be defined accurately

[1] The secchi method is a simple way to measure water clarity. A bright plate called secchi plate is lowered into the water and when it is not visible anymore the secchi depth is found.

for when successful ALB surveys can be conducted. Because water surface conditions are different at each survey site, due to earlier and present weather conditions, the study must be able to adjust to those conditions.

1.2 Goal of the investigation

The main focus of this project has been to develop a method that can take different environmental conditions into account and describe how they affect the directions of the laser beam due to the ocean surface. To do this a software able to create realistic height maps of ocean surfaces, perform ray tracing of a laser beam intersecting the surfaces and extract the statistics from the data, was developed.

The software was used to study the effects on important parameters when conducting ALB surveys. One of the most important parameters when evaluating the refraction of the laser beam due to the wave surface condition is the change of the average main direction when looking at several pulses. Knowledge about how the average main direction differs from the case when the surface is flat is important for depth accuracy. The goal was to see if information about the surface conditions could be used in order to make a better estimate of the new average main direction.

When looking at the average direction for each single beam, another important parameter to gain knowledge about, is how much variability one can expect from the average main direction discussed above. Insights about how this variability depends on the water surface conditions will provide useful information about the horizontal accuracy when conducting an ALB survey.

Finally, how much the light directions - within each laser pulse - are likely to deviate is also of interest. This gives information about how the confinement of the refracted laser beam varies and thereby enabling to estimate the probability of detecting objects of different sizes on the sea floor.

1.3 Outline

The report is divided into seven different chapters: introduction, airborne lidar bathymetry, description of the ocean surface, investigation methodology, generation of 3D surfaces, measurements and simulations, and results and discussion.

The method behind ALB is described in the second chapter. It is meant as a brief guide to those readers who are not familiar with ALB and the focus is on the basic principles rather than specific technological solutions. The problems rising from a non flat surface is enlightened in order to explain the purpose of this study.

The third chapter briefly describes topics important to understand the shape of the ocean surface. It starts with some general laws of physics and the environmental parameters affecting the ocean surface appearance. It is followed by a section about how to describe the ocean surface using statistical methods. The final section gives a detailed explanation of how one of the most comprehensive surface models available can be interpreted.

Chapter 4 focuses on how the theoretical and empirical investigations were conducted. It starts with narrowing down the field of study so that the investi-

gation will be conducted using the same conditions as when real ALB surveys are done. Then the theoretical method of investigation is explained. Empirical work was conducted in order to evaluate the results from the theoretical study and this is described in the last part.

In the fifth chapter a detailed explanation is given of how to construct realistic looking ocean surfaces as as triangulated irregular network (TIN). This is a vital part of the simulation work and the chapter is intended to serve as a detailed guide for everyone interested in creating realistic ocean surfaces based on physical models. The topic has previously been briefly described in other texts but a detailed guide intended for the unexperienced user has not yet been presented.

Chapter 6 presents the results from both the theoretical and the experimental studies. Explanation is given of how to prepare the data - from both studies - before analysis and how the analysis is performed.

In the seventh chapter the results are discussed by comparing the theoretical study with the empirical one as well as with other studies. Finally, the work is summarized and methods to continue with future research are discussed.

Chapter 2

Airborne Lidar Bathymetry

2.1 Coastal Mapping

The need for a time- and cost-effective method to map coastal areas is huge. As declared by the intergovernmental organization, International Hydrographic Organization (IHO), it is of great importance for a safe use of the sea, national economic prosperity and for marine environmental protection. IHO also states that nautical charting - in many areas of the world - is insufficient and capacity building is needed[1].

The most frequently employed method when mapping the ocean is using a multi-beam sonar mounted on a ship. The method, which was developed in the late 1950's, sweeps the sea floor with the use of directed acoustic pulses. The pulses are aimed in a grid pattern with a size dependent on the maximum sweep angle of the multi beam sonar and the water depth. The technique has been proven effective at deeper waters. At shallower waters the surveys are however time consuming and therefore also expensive since the coverage rate diminishes with diminishing water depth. There is also an increasing time aspect rising from the fact that in coastal areas there are often a lot of obstacles forcing the survey vessel into complicated and sometimes also dangerous maneuvering.

ALB provides the solution for surveying those shallower coastal areas. Instead of acoustic pulses, as in a multi-beam sonar, the ALB system uses laser pulses when scanning the sea floor. By mounting the ALB system on an aircraft the coverage rate increases and effective surveys can be done. There is no need to do to much of maneuvering around small islands and islets. As a matter of fact many ALB systems can simultaneously provide information about topography as well. Seamless charting can then be created between topographic and bathymetric features. In Figure 2.1 the difference in coverage, between multi-beam sonar and ALB, at shallow waters is exemplified. Also the seamless charting of land and sea floor is presented.

ALB is more effective in shallow and intermediate water depths due to the increased attenuation of the laser light in long path lengths of water meaning that the multi-beam sonar has the possibility to survey deeper regions than an ALB system. Therefore multi-beam sonar and ALB are not two competitive techniques but instead complement each other.

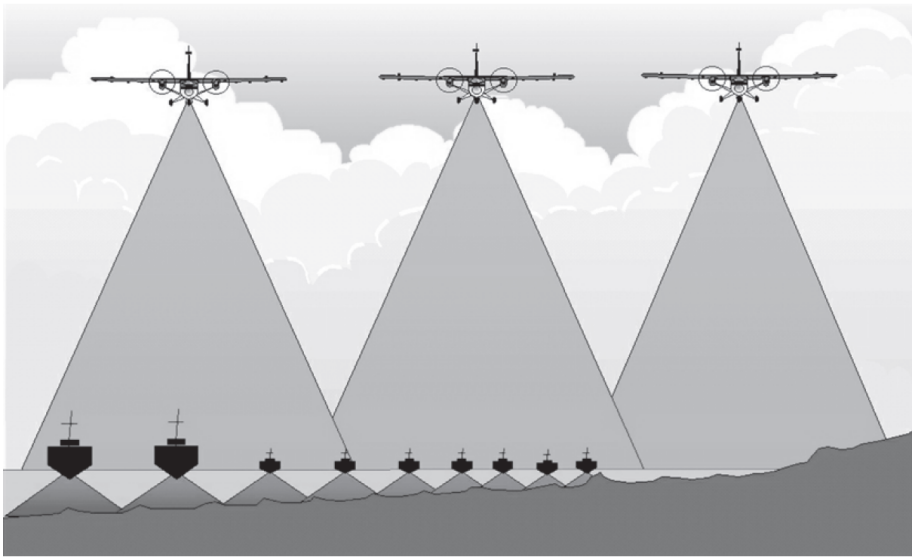

Figure 2.1: In shallow areas, the coverage for a multibeam sonar diminishes. The ALB system has a much better coverage in those waters and can also provide seamless topographic charting at the same time[2].

2.2 How an ALB system operates

The ALB system works by launching short pulsed laser beams towards the water surface. A portion of this light will be reflected at the air/water interface and some of that will be returning to the system. However, a large part of the light penetrates the surface and new directions of the light are introduced according to Snell's law of refraction. Depending on the water clarity some amount of volume backscattering will occur when the light continues to propagate through the water column before reaching the sea floor. At the sea floor the light will be reflected and some of it will propagate back, up to the water surface. Here refraction will occur again and some of this light will be returning to the ALB system.

The ALB system is recording the part of the pulse that gets reflected back resulting in a big intensity peak caused by the surface reflection and a smaller one from the sea floor reflection. By measuring the time difference between the two peaks and knowing the initial angle of incidence the distance between the water surface and the sea floor can be calculated. Figure 2.2 shows a schematic picture of this process.

There are several aspects affecting the cover rate of a survey. The pulsed laser is aimed in a sweeping pattern towards the surface with the result that each pulse illuminates an individual part of the sea floor, as shown in Figure 2.3. The spacing, a, between the illuminated parts within a sweep can be adjusted in order to meet requirements of how dense the mapping should be. Parameters to control this are the repetition rate of the laser, the sweeping speed and the altitude, H, of the aircraft. The altitude of the aircraft also affects the swath

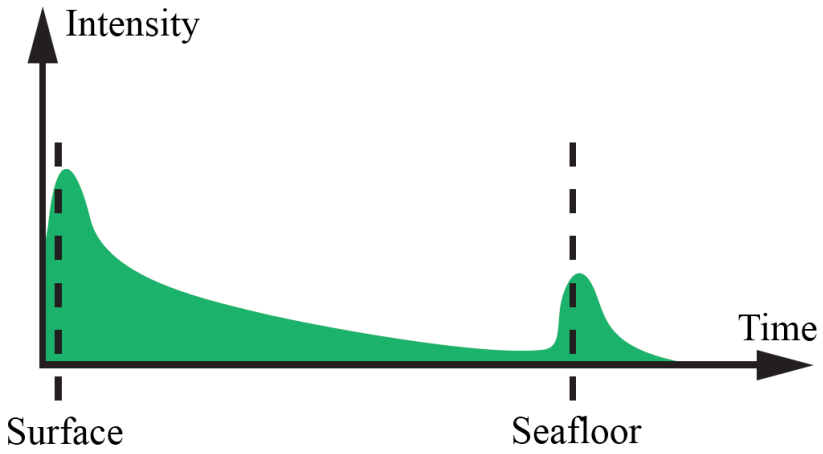

Figure 2.2: Schematic picture of the backscattered light in respect to time. The time between the two peak gives the distance from the surface to the sea floor [2].

distance, S, of each sweep which is of importance for the total survey time. In the flight direction the resolution is affected by the velocity, v, of the aircraft. The velocity is also an important factor for the total survey time. It is obvious that there is a trade-off between resolution of the survey and the total survey time.

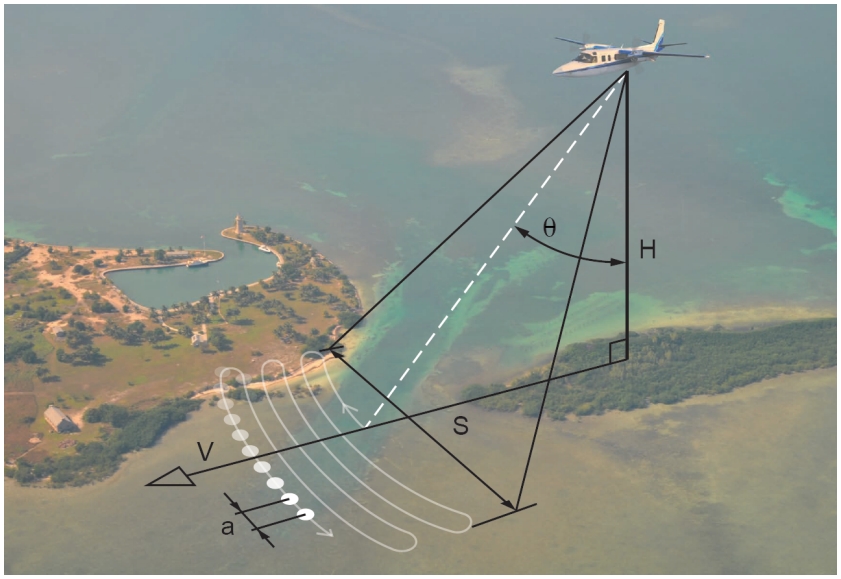

Figure 2.3: Schematic picture of how a ALB survey is conducted[3].

2.2.1 Parameters affecting the accuracy

The basic principle behind the ALB system is easy but the difficult task is to get every single part of the system to work synchronously. The overall accuracy is a result of the contributions to the accuracy from every individual part. For example, knowing the exact position of the aircraft demands accuracy in the GPS system, measuring roll and pitch of the aircraft accurately determines the aiming accuracy of the pulse, receiver and digitizer are important for the timing measurements of the pulses, just to mention a few of the crucial parameters. Technological development continuously decreases the error introduced from these various aspects.

Another important parameter, not dependent to the ALB system itself, is the shape of the water surface illuminated by the ALB footprint. If the water would be perfectly flat, Snell's law could be used in the same way on every single part of the beam and there would be no difficulties calculating the new direction of the refracted laser light. However, a non-flat surface which is most often the case will complicate the picture.

As the transmitted laser beam reaches the water, it broadens proportional to its beam divergence and covers a typical area of 3-6 m in diameter depending on the flight altitude, H. As an example the Hawk Eye 2 system, developed by AHAB, creates a laser footprint on the surface with a diameter of 4.5 m when flying at an altitude of 300 m. The waves, generated by the wind at the area of survey range from less than a centimeter up to meters in amplitude. As a result, the laser beam interacts with multiple facets that redirect the light into several different directions. Assuming a laser beam with a Gaussian cross-section, surface slopes located at the center of the beam will interact with larger amount of energy compared to slopes located at the periphery. The result after the air/water interface will be a distorted footprint of the laser beam and most likely a new main direction of propagation.

Since the pulses are aimed at different locations on the water surface, due to the sweeping pattern, the shape of the intersected air/water interface will differ from pulse to pulse and as a result of this the new directions of the beams will vary accordingly.

Figures 2.4 and 2.5 visualizes the problem. For a given depth, z, and a given nadir angle, φ, the light will be traveling a distance, R_1, in the water before hitting the sea floor. If the nadir angle is wrong by $\Delta\varphi$ the light will instead be traveling a distance R_2.

This yields an error in the light path distance denoted ΔR. Since the exact direction of every pulse cannot be known one will use nadir angle φ when calculating the water depth because this is the best estimate. ΔR introduces a horizontal error Δx depending on the angle deviation and water depth as shown in Table 2.1. ΔR also yields a vertical error for the same reasons as shown in Figure 2.5 and Table 2.2.

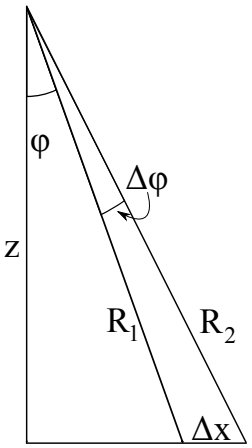

Figure 2.4: A direction error $\Delta\varphi$ introduces an error in the traveling distance in water causing a horizontal error, Δx.

		Depth (m)		
		10	**20**	**30**
Deviation	**0.5**	8.7	17.5	26.2
angle	**1.0**	17.5	34.9	52.4
(degrees)	**1.5**	26.2	52.4	78.5
	2.0	34.9	69.8	104.7

Table 2.1: The horizontal error, Δx, expressed in cm for different water depths and deviations angles, $\Delta\varphi$. Original direction $\varphi = 15$ degrees.

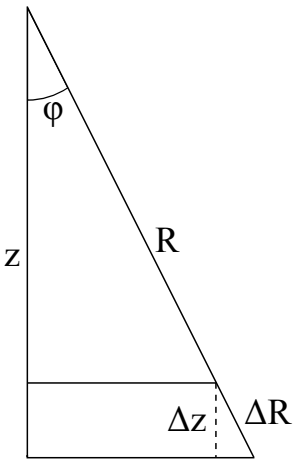

Figure 2.5: An error in the traveling distance in water introduces a vertical error, Δz.

		Depth (m)		
		10	**20**	**30**
Deviation	**0.5**	2.3	4.7	7.0
angle	**1.0**	4.7	9.4	14.0
(degrees)	**1.5**	7.0	14.0	21.0
	2.0	9.4	18.7	28.1

Table 2.2: The vertical error, Δz, expressed in cm for different water depths and deviations angles, $\Delta\varphi$. Original direction $\varphi = 15$ degrees.

Some investigations about the slope distribution of the ocean surface and how it effects the laser beam have been done. The experiments conducted by Cox and Munk (1954) where photos of sun glitter were studied are one of the largest contributions and often cited[4]. Guenther states that from those measurement an estimated horizontal error of ± 0.36 m RMS per 10 m of water depth is reasonable for wind speeds of 10 knots[2]. This is, however, a somewhat crude estimate and further investigations of how the surface affects the accuracy need to be done.

Except from mapping the sea floor, another important aspect for ALB surveys is to locate individual objects that can be hazardous for marine traffic. Examples could be sharp subsurface rocks, masts, from shipwrecks or mines. One of the most important parameters, affecting the probability of detection, is how dense the pulses are aimed at the surface. However, the ocean surface is also important since it changes the direction of the pulses and the shape of the laser footprint on the sea floor. Even though the main direction remains unchanged the shape of the footprint can differ vastly causing some objects, to remain undetected.

This thesis intends to add additional information and provide a broader picture both regarding the main direction pulse and also the probability of target detection. In order to do so knowledge about the ocean surface is vital.

Chapter 3

Describing the Ocean Surface

The theory of how to describe the structure of the ocean surface has been of interest for science and engineering for a long time. The need for a mathematical description of the ocean is present in many areas like engineering coastal structures able to handle the waves occuring in the area, handling backscattering from the surface when using radar measurement techniques or simulating ocean water in computer software[6][7]. Many different approaches of describing the ocean surface have been invented through the years and depending on the reason for conduct a certain study, different models are useful. The complexity varies from simple relations that can be evaluated with pen and paper to extremely complex simulations taking into account many different environmental parameters and making use of a large amount of computational power. All these approaches are not of interest for this thesis and will not be described. One of the more commons methods have however been used and constitute a major part in this study. This method will therefore be described in detail later in this chapter.

3.1 General

When a disturbing force acts on flat water, surface waves are generated. Throwing a stone in a pond or driving a boat on a lake are two common examples of generating surface waves. Another common example is wind blowing over a flat surface giving rise to small ripples.

There are also forces trying to restore the flat surface. If the wave is larger than 1.7 cm the dominating restoring force is gravity and those waves are therefore called gravity waves[8]. If the wave is smaller than 1.7 cm the dominating restoring force is surface tension. Those waves are called capillary waves. It is common that a disturbing force introduces waves over a spectra and therefore both types of waves are often present.

When looking at the ocean surface it is obvious that a complete mathematical description is not trivial to do. In fact, there is yet no theory that completely can describe every part of ocean surface phenomena[9][10]. The shape of the ocean changes constantly and sizes of the wind generated waves range from only a few millimeters up to several hundred meters or more[11]. Depending on the strength of the wind, different sizes of waves will be generated giving the

shape a wind dependence. Due to wave dispersion, waves at different sizes travel with different speed, which leads to a time or distance dependence. Another parameter affecting the speed of the waves, and also the shape of them, is the water depth[8]. Also, different groups of waves can interact with each other, which is most often the case[10], giving rise to interference making the picture even more complicated. A complete ocean surface theory should be able to take all those parameters and much more into account.

3.1.1 Wind generated waves

In this study, the only disturbing force that will be considered is the wind. The wind is the main contribution to disturbance of the sea surface and is more or less affecting all off the sites were ALB surveys are conducted. Other disturbing forces are often negligible in comparison or very rarely occurring.

When the wind starts to blow, on a completely flat surface, small ripples start to appear. If the wind is blowing over a distance those ripples will develop into larger waves since the wind will continue to transfer energy to the waves. The wave size will increase up to a certain level where an equilibrium is reached. When that occurs it means that the wind cannot provide the surface with more energy than what is dissipated by the ocean at the same time. The most obvious example of dissipation mechanism is wave breaking but there are also internal mechanisms within the wave[10]. Higher wind speeds leads to larger wave sizes before equilibrium is reached. When equilibrium occurs one says that the sea is fully developed.

The ocean surface is often described in sea states where different wind speeds relate to wave appearance according to the Beaufort scale[8]. The different states ranges from zero when no wind is blowing and the surface is perfectly flat up to state twelve with huge waves generated by the winds from e.g. a hurricane.

The Beaufort scale assumes fully developed sea. In many occasions the time or the distance were the wind is blowing have not been sufficient for a fully developed sea to develop. This might occur if the observation is done close to the shoreline and the wind is coming from land, or in case of a weather change. This distance over which the wind is blowing is called fetch and it is a very important parameter when describing the wind dependence of the surface.

There might also be waves present that have been generated by weather systems outside the area of interest. Those waves are called swells and can travel large distances across entire oceans. Due to wave dispersion of water waves, large waves travel faster than smaller waves causing waves from the same weather system to arrive at different times. Therefore swells often consist of single frequency waves making them somewhat easier to estimate. Large waves lose less energy than smaller waves when propagating for a long distance[10]. A consequence is that swells often tend to have wavelengths larger than the waves generated by the winds at the present location for moderate wind speeds.

3.1.2 Water depth

Another important parameter for the wave behavior is the water depth. Imagine a tiny particle just beneath the surface in a wave over deep water. When studying the motion of the particle one will find that it is almost perfectly circular. The diameter of the circular path is the same as the wave height and

it moves forward when it is at the crest of the wave and the opposite direction when it is at the through. The shape of the orbital motion is preserved if the particle would be situated deeper but the diameter of the path decreases exponentially in relation to the depth. When distance up to the surface is more than half the wavelength the diameter of the motion is negligible[8]. The wave profile in those waters can be considered well described by sinusoidal equations and linear relations e.g. superposition can be used. This is the so called Airy theory after the inventor or the Linear theory[6].

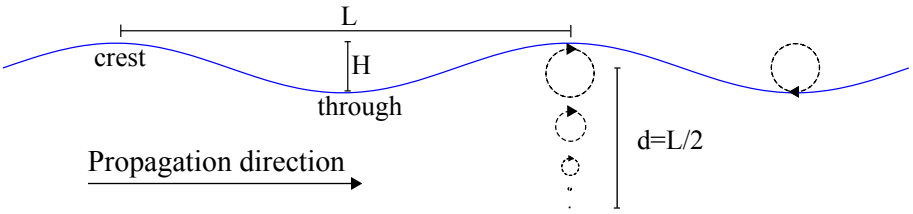

Figure 3.1: A simple description of the most basic wave parameters and the circular motion of a particle.

When the water depth is smaller than half the wavelength the orbital motion can no longer be considered circular but rather elliptical and one can no longer assume that the Linear theory is valid. There are theories able to describe even shallow waters but the mathematical description starts to get too complex for this study.

The size of the wave is related to the wind and is therefore also described by the sea state meaning that the Linear theory can be used to describe waves relatively close to the shore line as long as the sea state is not too high. The upper limit for the waves due to the wind speed at the location will therefore give us a lower limit for the water depth. The wavelength of the largest wave divided by two is often used as a threshold value for when the water can be considered deep. The threshold origins from the relation of how the celerity, c, or phase speed of a water wave is calculated. It is described by

$$c = \sqrt{\frac{gL}{2\pi} \tanh\left(\frac{2\pi d}{L}\right)}$$

where g is the gravity constant, L is the wavelength and d is the depth. When $d \geq L/2$ one gets $\tanh(2\pi d/L) \approx 1$ giving

$$c \approx \sqrt{\frac{gL}{2\pi}} \tag{3.1}$$

showing that the depth dependence is lost. Swells are, as mentioned, often the largest wave.

3.2 Statistical approach

One popular way to describe the surface over deep waters is to assume that it is made up of many different random single frequency plane waves. The

waves which have a sinusoidal shape have different amplitude, wavelength and phase and by combining many of those an ocean surface can be described. The theory is called random linear wave theory[12] and origins from signal theory. Figure 3.2 describes how three different single frequency signals with different frequency, amplitude and phase are combined into a more complicated signal using superposition. It is easy to understand that when the number of single frequency waves become large more complex waves can be constructed.

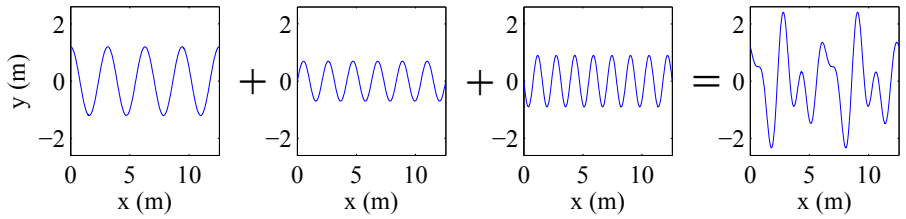

Figure 3.2: Three single frequency signals building up a more complex signal with the use of superposition.

The method makes use of the Fourier theorem that says that every signal can be described as a combination of single frequency signals[13]. The signals so far have been described in one dimension, i.e. time dependent and along a straight line but the Fourier theorem also holds for higher dimensions. In the specific case with the ocean surface, the surface elevation is a function of the coordinates x and y and therefore the single frequency signals also needs to be dependent of x and y[12]. Figure 3.3 describes three single frequency plane waves in three dimensions building up a simple surface.

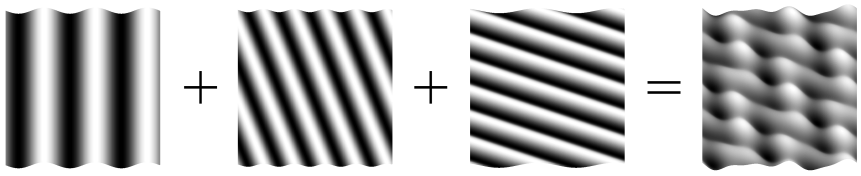

Figure 3.3: Three single frequency surfaces building up a more complicated surface.

This method of describing the ocean has through the years proven to be one of the more far reaching methods and a lot of work has been done within the field[10].

One of the benefits with this method is that the surface can be described by the use of spectral analysis. For this, wave spectrum distributions will be used were the distribution of the variance of the sea level is related to specific frequencies[10]. Another common name is the energy spectrum since it is easily related to energy by multiplication by the density ρ and the gravity constant g.

It is also often simply called the wave spectrum[10]. In this thesis will use the term wave spectrum since energy spectrum might be somewhat misleading.

Different ocean states have different wave spectra telling us what frequencies that are likely to occur and how much energy they are likely to have. However since it is a probability distribution there is no guarantee that the sea state at a specific time is perfectly represented by the wave spectrum. This is actually highly unlikely. The combined result of many measurements will however provide a relation according to the wave spectrum.

The wave spectrum of an ocean surface is measured by recording the ocean elevation for a time much longer than the longest wave period one would like to be able to detect. Those measurements are then translated into the frequency domain using Fourier transform. There is a wealth of measurements conducted in all kind of different environments. However, a an important goal for the oceanographic society is to find a model able to describe the wave spectrum related to specific environmental parameters.

3.3 Wave spectrum models

Knowing the wave spectrum provides a huge amount of information about the surface. There are however many occasions were direct measurements of the spectrum cannot be done or the impact from specific environmental parameters are to be studied in detail. A lot of effort has been put into the development of models able to recreate the wave spectrum according to different environmental input parameters. Major interesting parameters to take into account are the wind speed above the surface and fetch i.e. the distance the wind is blowing over the surface and water depth. The complexity of the models varies a lot depending on input parameters and approach.

3.3.1 One-dimensional spectrum

The idea of describing the surface by a spectral formulation originates from Phillips (1958)[14] and Rice (1945)[15][10]. Phillips formulated an equilibrium relation between the wave spectrum and the angular frequency, ω, assuming that the wind has been blowing for a long time and over a large distance giving a fully developed sea and that the water is deep.

$$S_P(\omega) = \alpha g^2 \omega^{-5} \tag{3.2}$$

α is called the Phillips constant with a value of 0.0081 and variations of it are used in many other wave spectrum models. Equation 3.2 has been the starting point for many following wave spectrum models, including the ones used in this study. In 1964 *Pierson* and *Moskowitz* presented a wave spectrum model with dependence on the wind speed $V_{19.5}$, measured 19.5 m above the surface and the frequency, f.[16] The spectrum model will be denoted as the PM-spectrum. The sea is still assumed to be fully developed and deep.

$$S_{PM}(f) = \frac{\alpha g^2}{(2\pi)^4 f^5} e^{-0.74\left(\frac{g}{2\pi V_{19.5} f}\right)^4} \tag{3.3}$$

Figure 3.4 shows the wavenumber version of the one dimensional spectrum parallel to the wind for three different wind speeds.

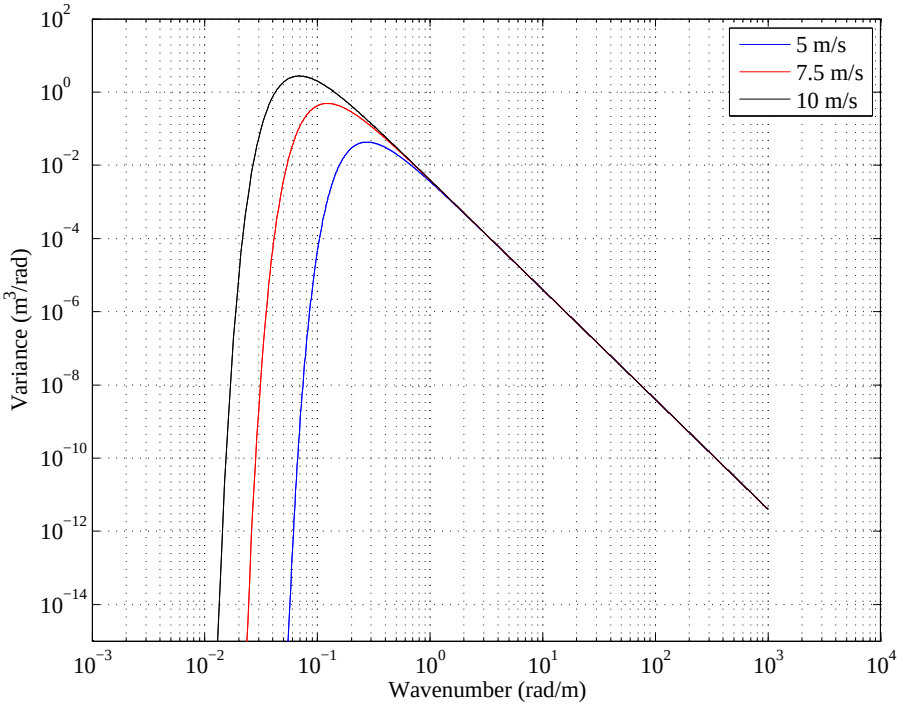

Figure 3.4: The PM-spectrum for three different wind speeds.

The equation is rather simple but serves as a good example for introduction to wave spectrum models. It has fairly good agreement with the Beaufort scale for large winds and waves but is not suitable when smaller waves are considered. The spectrum, which has been one of the most used wave spectrum models, is still in use for example within the computer graphics industry[10][5]. In Section 3.4 a more advanced and up-to-date wave spectrum model able to describe a larger range of wave frequencies will be covered in detail.

3.3.2 Angular spreading

The one dimensional spectrum is the most common one. When a three dimensional surface is of interest an additional relation is needed describing the spreading of the frequencies relative to the wind direction. A common name is angular spreading function or directional distribution function. As for the directional spectrum there are plenty of angular spreading models available with various complexity. One of the simpler ones is defined as

$$\Phi(\varphi) = \frac{2}{\pi}\cos(\varphi)^2, \qquad |\varphi| < \frac{\pi}{2} \tag{3.4}$$

where φ is the direction in comparison with wind direction[10]. Figure 3.5 shows the spreading function expressed in a polar plot.

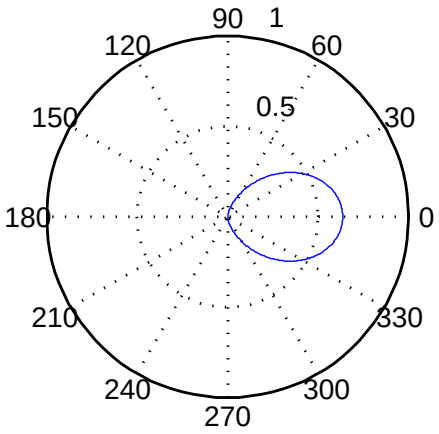

Figure 3.5: A simple version of an angular spreading function. Wind direction at zero degrees.

By multiplying the one dimensional spectrum with the angular spreading function one gets what is called the directional wave spectrum.

$$S(f, \varphi) = S(f) \cdot \Phi(f, \varphi) \tag{3.5}$$

Integrating the directional wave spectrum over all directions should give us the one-dimensional wave spectrum i.e.

$$S(f) = \int_{-\pi}^{\pi} S(f, \varphi) d\varphi \tag{3.6}$$

yielding

$$\int_{-\pi}^{\pi} \Phi(f, \varphi) d\varphi = 1 \tag{3.7}$$

3.3.3 Converting spectra into wavenumber domain

Most wave spectra are expressed as a relation of frequency, f, or angular frequency, ω. However, in this study the spatial information is of interest rather then the time information. Thus, a method is needed for converting the spectra to be related to the wavenumber, k, instead. The conversion must follow the integral relation

$$\int S_f(f) df = \int S_k(k) dk \tag{3.8}$$

One can relate k and f by starting with Equation 3.1 expressing the celerity, c as a function of wavelength. The celerity of a wave is the time, T, it takes for one

wave of wave length, L, to pass a fixed point giving $c = L/T$[8]. Substituting c in Equation 3.1 and using $T = 1/f$ gives

$$L = \frac{gT^2}{2\pi} = \frac{g}{2\pi f^2} = \frac{2\pi}{k} \qquad \text{and} \qquad f = \frac{\sqrt{gk}}{2\pi} \tag{3.9}$$

The conversion is then done by

$$\int S_k(k)dk = \int S_f(f)df = \int S_f(f(k))\frac{df}{dk}dk \tag{3.10}$$

where

$$\frac{df}{dk} = \frac{1}{2\pi}\sqrt{\frac{g}{k}} \tag{3.11}$$

giving

$$S_k(k) = S_f\left(\frac{\sqrt{gk}}{4\pi}\right)\frac{1}{2\pi}\sqrt{\frac{g}{k}} \tag{3.12}$$

The same principles hold when converting from an angular frequency spectrum.

This method of creating a directional spectrum gives us the building block when constructing realistic ocean surfaces later on. However, the PM-spectrum is one of the earliest models and more modern models able to recreate wave spectrum with better consistency with natural waters are available. The model used in this study was developed by Elhouhaily et al. and is called *A unified directional spectrum for long and short wind-driven waves* [7]. In the text it will be referred to as the ECKV model after the first letter in the family names of the authors.

3.4 The ECKV wave spectrum model

The key aspect for choosing the ECKV model is its ability to produce a spectrum over a broad range. Many other spectra are valid for large waves but lack the properties for smaller waves or vice verse. In the study it is important that the range from small capillary waves to medium sized gravity waves is covered since this is often the case when conducting ALB surveys. Another important aspect is its consistency with observations from nature e.g. the sun glitter experiments by *Cox and Munk* in 1954.

The ECKV model is based on several other earlier models and not empirical data. Instead the focus has been to combine models and make them consistent with earlier studies. The relation is rather complex and the two following sections intend to explain how the spectrum model is supposed to be used. For learning about how the model was constructed the readers are recommended to read the original article as well.

3.4.1 One-dimensional wave spectrum ECKV model

As mentioned in Section 3.3 a directional spectrum $S(k, \varphi)$ consists of one part representing the one-dimensional distribution $S(k)$ and one part representing the angular spreading $\Phi(k, \varphi)$. In the ECKV model the one-dimensional distribution $S(k)$ is separated into two parts.

$$S(k) = \frac{1}{k^3}(B_l + B_h) \tag{3.13}$$

B_l is the long-wave curvature spectrum and B_h is the short-wave curvature spectrum. Both can be broken down into several different sections. Starting with the long-wave curvature spectrum

$$B_l = \frac{\alpha_p}{2} \cdot \frac{c_p}{c(k)} \cdot F_p \tag{3.14}$$

where α_p is the Phillips-Kitaigorodskii equilibrium range parameter for long waves. It is related to the Phillips constant mentioned earlier and is dependent on the inverse-wave-age parameter, Ω, by

$$\alpha_p = 0.006\sqrt{\Omega}$$

The inverse-wave-age parameter will be explained below. c is the celerity of the wave, here related to k using $c = \sqrt{g/k}$. c_p is the celerity of the wave with the wave number k_p at the spectral peak. Those waves are sometimes called the dominating waves. The spectral peak wave number is related to the wind speed V_{10}, ten meter above the surface, and to the inverse-wave-age parameter by Equation 3.15

$$k_p = g\left(\frac{\Omega}{V_{10}}\right)^2 \tag{3.15}$$

The inverse-wave-age parameter Ω mentioned above relates to the fetch size x of the spectrum by

$$\Omega = \tanh\left(\left(\frac{g \cdot x}{22000 \cdot V_{10}}\right)^{0.4}\right)^{-0.75} \tag{3.16}$$

Continuing with Equation 3.14, F_p is the long-wave side effect function which is defined by

$$F_P = L_{PM} \cdot J_P \cdot \exp\left(-\frac{\Omega}{\sqrt{10}}\left(\sqrt{\frac{k}{k_p}} - 1\right)\right) \tag{3.17}$$

It limits the energy for higher wave numbers. This shows that the ECKV model is constructed by combining earlier results. L_{PM} is the standard Pierson-Moskowitz function given by

$$L_{PM} = \exp\left(-\frac{5k^2}{4k_p^2}\right) \tag{3.18}$$

It origins from Equation 3.3 from the earlier mentioned Pierson-Moskowitz spectrum from 1964. Another very reputable spectrum is the JONSWAP spectrum from 1973 derived by Hasselman et. al. after conducting extensive measurements in the North Sea[16]. J_P in Equation 3.17 is the JONSWAP peak enhancement function defined as

$$J_P = \gamma^\Gamma, \qquad \gamma = \begin{cases} 1.7 & 0.84 < \Omega < 1 \\ 1.7 + 6\log(\Omega) & 1 < \Omega < 5 \end{cases} \tag{3.19}$$

$$\Gamma = \exp\left\{ -\frac{\left(\sqrt{\frac{k}{k_p}} - 1\right)^2}{0.0128\left(1 + \frac{4}{\Omega^3}\right)^2} \right\} \tag{3.20}$$

The peak enhancement factor modifies the shape of the PM-spectrum shape making the peak sharper and higher and further relating the shape of the spectrum to the fetch size.

That concludes all parts for the long-wave curvature spectrum. There is no need to put all parts together in this text. Thus this has been further developed in the appendix. When conducting the simulations the different parts, as expressed here, were calculated separately and then combined.

The short-wave curvature spectrum is somewhat similar to the long-wave curvature spectrum and described by

$$B_h = \frac{\alpha_m}{2} \cdot \frac{c_m}{c(k)} \cdot F_m \tag{3.21}$$

where α_m is the Phillips-Kitaigorodskii equillibrium range parameter for short waves, explained further below. c_m is the minimum phase speed at wavenumber k_m which is $c_m = \sqrt{2g/k_m} = 0.23$ m/s. F_m is the short-wave side effect function

$$F_m = L_{PM} \cdot J_P \cdot \exp\left(-\frac{1}{4}\left(\frac{k}{k_m} - 1\right)^2\right) \tag{3.22}$$

In the original text, L_{PM} and J_P has gone missing. The Phillips-Kitaigorodskii equillibrium range parameter for short waves, α_m, in Equation 3.21 is expressed as a two-regime law

$$\alpha_m = \begin{cases} 0.01\left(1 + \ln(u^*/c_m)\right) & \text{for } u^* < c_m \\ 0.01\left(1 + 3\ln(u^*/c_m)\right) & \text{for } c_m < u^* \end{cases} \tag{3.23}$$

where u^* is the friction velocity at the water surface described by

$$u^* = 0.42\frac{V_{10}}{\ln(10/z_0)}, \qquad z_0 = 3.7 \cdot 10^{-5}\frac{V_{10}^2}{g} \cdot \left(\frac{V_{10}}{c_p}\right)^{0.9} \tag{3.24}$$

Finally, all parts of the one directional spectrum have been covered, and can be combined for investigation of the result. Figure 3.6 shows the spectrum for wind speeds ranging from 3 m/s to 21 m/s. Comparing with the PM-spectrum and Figure 3.4, it shows a difference especially for high frequencies where the spectrum have a different appearance for different wind speeds. Since there is no direction information in Equation 3.13, all directions will look the same when visualizing the results over the entire spectral domain as show in Figure 3.7

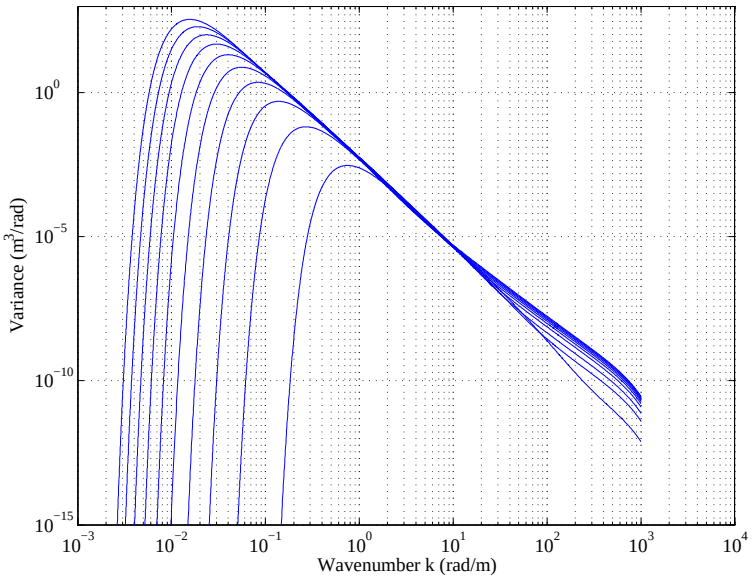

Figure 3.6: The one-dimensional ECKV spectrum received from Equation 3.13. Wind speed ranging from 3 m/s to 21 m/s.

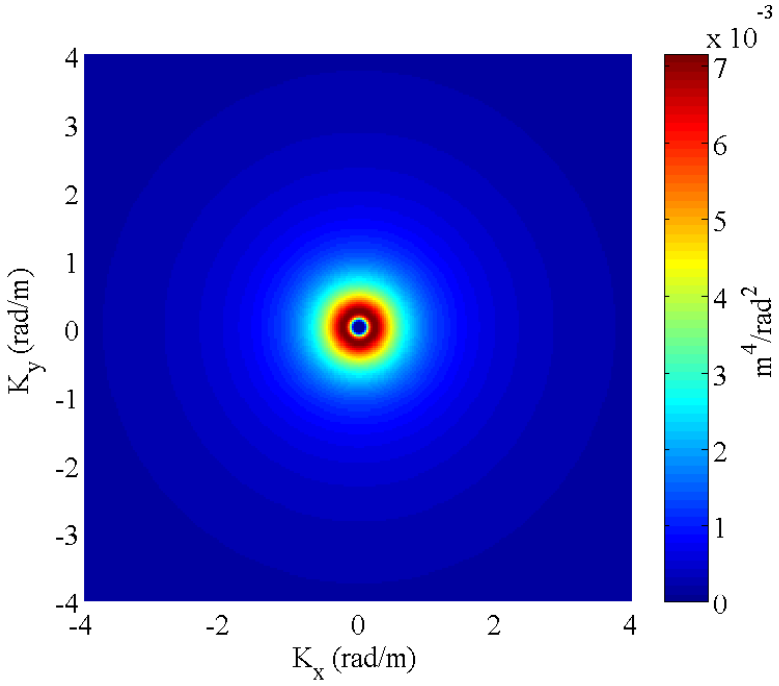

Figure 3.7: The one-dimensional wave spectrum visualized over the entire spectral domain.

3.4.2 Angular spreading function ECKV model

The angular spreading function $\Phi(k, \varphi)$ in the ECKV model, where φ is the angle to the wind direction, is defined as

$$\Phi(k, \varphi) = \frac{1}{2\pi}(1 + \Delta k \cos(2\varphi)) \tag{3.25}$$

where Δk is

$$\Delta k = \tanh\left(\frac{\ln(2)}{4} + 4\left(\frac{c}{c_p}\right)^{2.5} + a_m\left(\frac{c}{c_m}\right)^{-2.5}\right) \tag{3.26}$$

and

$$a_m = 0.13\frac{u^*}{c_m} \tag{3.27}$$

Unlike simpler angular spreading functions this gives a dependence on k. As for the one-dimensional spectrum, the angular spreading function is visualized for the entire spectral domain shown in Figure 3.8

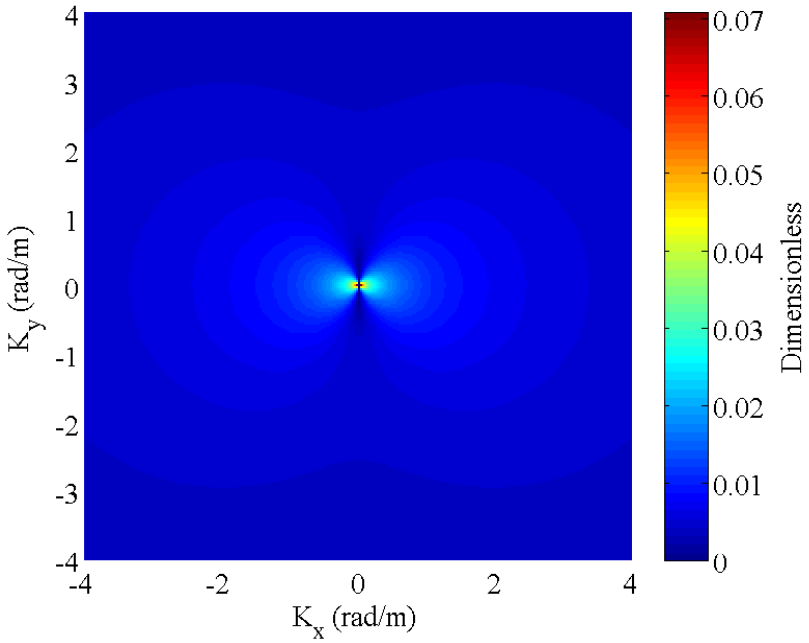

Figure 3.8: The angular spreading function from the ECKV model in the spectral domain.

The angular spreading function is dependent on both direction and absolute value of the wavenumber. The spectral domain is symmetric along the wind direction which is along the x-axis.

3.4.3 The directional spectrum

Combining Equation 3.13 and 3.25 gives us finally the complete directional spectrum $S(k, \varphi)$

$$S(k, \varphi) = \frac{1}{k^4}(B_l + B_h)\frac{1}{2\pi}(1 + \Delta k \cos(2\varphi)) \tag{3.28}$$

The effect of this multiplication is clearly seen in the spectral domain

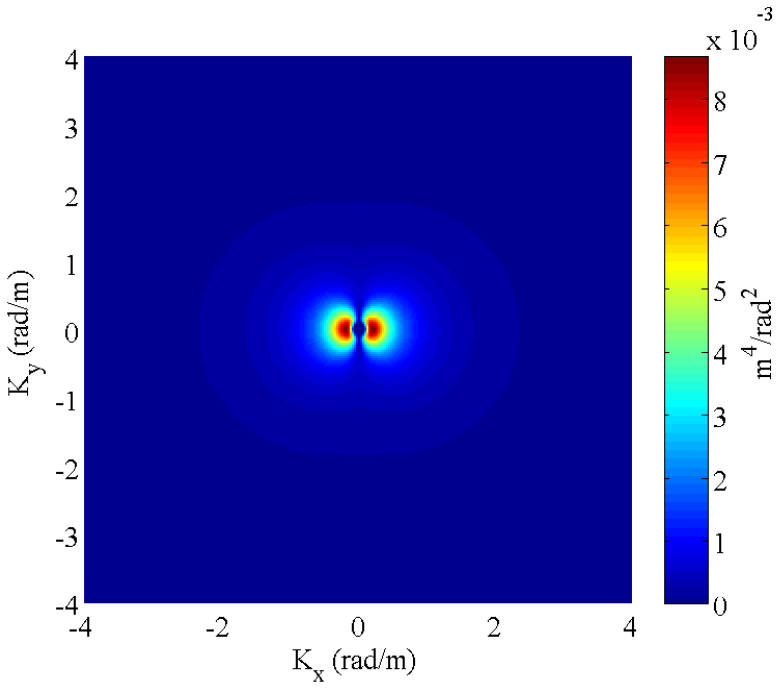

Figure 3.9: The directional spectrum.

This spectrum now fully describes the distribution of the variance of the surface elevation of a three-dimensional surface. It can be used for various investigation and will be used in chapter 5 when constructing realistic models of the ocean surface.

Chapter 4

Investigation methodology

When investigating how the direction of a laser pulse is changed due to the water surface, one theoretical study using a ray tracing approach as well as an experimental investigation conducting real measurement in a wave tank were chosen. The main part of the investigation consists of the theoretical approach, while the experimental measurement was done in order to be able to verify the theoretical results. Since the area is fairly unexplored a new method for conducting the studies had to be defined. This chapter describes how the parameters for the investigation were specified and how both the theoretical and experimental part were conducted.

4.1 ALB survey surface conditions

Since a theory describing every single case of the ocean surface is not available is it necessary to specify under what conditions the study can be conducted. Those conditions should as much as possible agree with the prevalent conditions when conducting ALB surveys. Even when they are narrowed down to those conditions they are too varied for this study and further simplification needs to be made.

When conducting an ALB survey it is important that a significant amount of the laser light penetrates through the water surface. One wave phenomena making this difficult is wave breaking. When the waves break, plenty of air bubbles are introduced just below the water surface. Those will scatter the light from the laser beam so much that the result from an ALB survey will be heavily affected. Since ALB surveys cannot be conducted when breaking is occurring this phenomena is therefore outside the scope of this study. According to the Beaufort scale a large amount of wave breaking starts to occur above sea state three giving us sea state three as the upper limit. This corresponds to wind speeds below 5.5 m/s. It is also confirmed by Guenther that ALB survey should not be conducted for wind speeds over 10 knots[2].

Since this gives have an upper limit for the wind speed one also needs to relate this speed to the waves generated at the location of interest. This is necessary because it determines a lower limit for the water depth were linear theory can be used. If the largest wave is 10 m then, according to the discussion leading to Equation 3.1, one can consider the water as deep if it the depth

exceeds 5 m. However, there is no simple way to determine the largest wave. Instead one looks at the energy spectrum and study for what wave numbers the major part of the energy is distributed. Since the spectrum has a step front and a large tail much of the energy will be at high frequencies. It was found that for the wave numbers between two thirds of the spectral peak frequency, k_p, and infinity holds 95 percent of the total energy. Thus, the largest wave is considered to have a wavenumber of $2k_p/3$. This gives a wavelength of

$$L_{max} = \frac{3\pi}{k_p} \tag{4.1}$$

were relations from 3.9 have been used. The spectral peak wavenumber, k_p, is dependent of the wind speed, V, and on the fetch size, x according to Equation 3.15 and 3.16 which therefore are the two limiting parameters. Figure 4.1 shows some examples of spectrum shapes for wind speed 5 m/s and different fetch sizes.

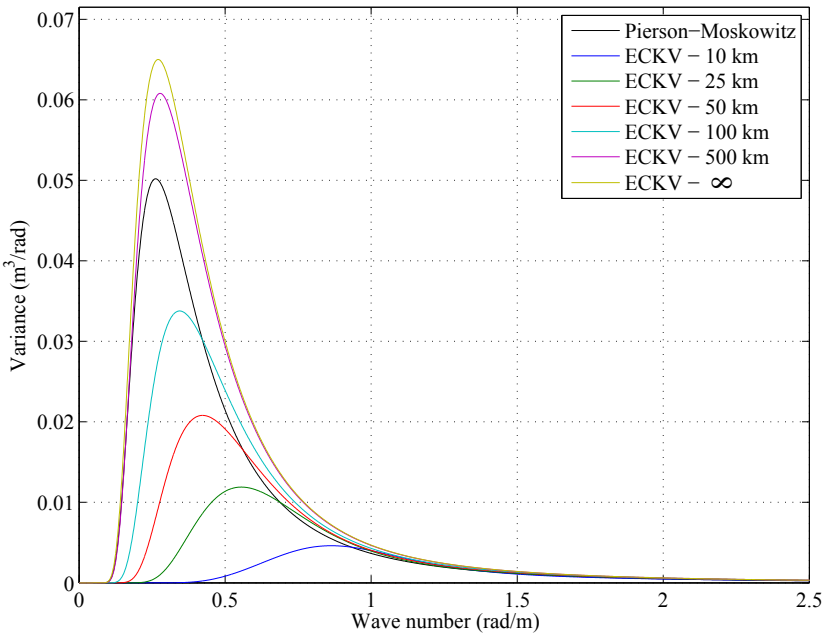

Figure 4.1: The shape of the spectrum changes due to fetch size. The spectrum increases i.e. contains more energy and the peak moves towards lower frequencies when the wind speed increases. The wind speed in this case was set to 5 m/s.

An increasing amount of energy and a spectral peak towards lower wave numbers is expected since a large fetch leads to higher and longer waves. The same holds for higher wind speeds. Figure 4.2 illustrates how wind speed and fetch size determines the smallest depth needed for linear theory to be valid.

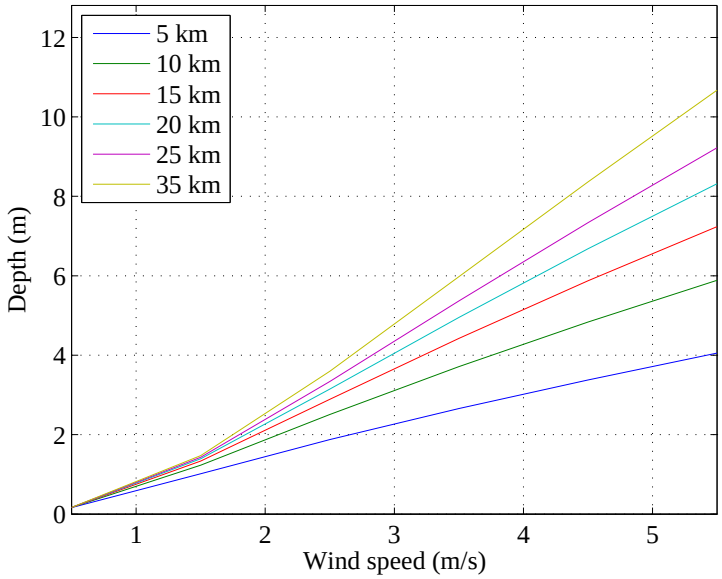

Figure 4.2: Minimum water depth for linear theory to be valid as a function of wind speed. The different lines represent different fetch sizes. The wind speed range is determined after ALB survey conditions.

If swells are to be taken into account this lower limit of depth has to adopt for those larger waves. In this study, the cases when waves from one or several nearby weather system interfere at the area of interest will not be covered.

4.2 Theoretical approach

When conducting the theoretical investigation, a method is needed where one as input uses known information about the laser pulse and the water surface and as output receives information about the refracted laser pulse. The method should be able to work for varying information about the surface and also varying information about the light source. The method of choice was to write a ray tracing software and simulate the propagation of single rays from a laser source down and through constructed water surface models.

In order for this to work, realistic water surface models needed to be created based on wave spectrum information. The methods to do so are described in Chapter 5. Structures consisting of millions of triangle facets were created and saved as Triangulated Irregular Network models (TIN). Those TIN models were then imported into the program and used as interfaces between air and water. Information about the propagated rays was stored and the changes of the laser beam due to the surface structures was investigated by comparing the directions of the rays before and after intersecting the surface.

The theoretical study focuses on two different cases. In the first case, the theoretical set-up s built to replicate the conditions from an operating ALB

survey system. Ocean surface structures were created according to the ECKV wave spectrum model for environmental conditions for real ALB surveys. The wind speed for different setups ranged from 3 m/s to 5.0 m/s and the fetch size ranged from 10 km to 10000 km. A fetch size of 10000 km is for the ECKV model equal to infinity. The direction of the waves in comparison to the wind was also alternated by turning the set-up 90 degrees. A study was also conducted where the size of the laser spot size, at the surface, was changed.

Pulsed laser beams with Gaussian cross-section were generated and launched. The Hawk Eye II system has a laser beam divergence of 14 mrad when using the $1/e^2$ beam size measuring convention and therefore the source was adjusted to meet those specifications. The altitude of the aircraft was set to 300 m. The usual nadir angle of the laser beam is 20 degrees giving us a distance between the laser and the intersection area of 320 m. This generates a footprint with a diameter of 4.5 m at the water surface.

In the second case, the theoretical set-up was built according to the arrangements used when the empirical measurements were conducted in the laboratory, which is described in Section 4.3. Laser specifications, set up dimensions and surface wave parameters were all set according to those conditions. By doing this, the theoretical results could later be evaluated using the empirical measurements.

The changes of the laser beam for many different surface structures could easily be studied. Thousands of rays, simulating one pulse, were generated and propagated through a surface structure and for each ray the data was recorded before and after the air/water interface. Then the surface was changed and an identical test was conducted with a new pulse. This process was repeated by a script many times simulating many pulses.

From the stored directions data, direction distribution plots, for each pulse, could be created describing statistical information about the main direction and the variability within each pulse. Putting the main directions for all pulses in a new plot will give a distribution of main directions and information about the new average main direction for all pulses and the variability of the main directions.

From the data one can also construct the shape of the laser footprint on the sea floor. Since the direction and the starting point is known, for all rays, one can decide the water depth of interest and study how the shape changes accordingly. By examining the amount of light, illuminating a particular part of the sea floor, and doing so for many pulses, a statistical data about the illumination ratio due to various water depths and environmental conditions will be gained. From this, the potential of target detection can be estimated.

4.3 Experimental approach

The empirical measurements were conducted at the facilities of the Center for Coastal and Ocean Mapping Center, located in the Chase Ocean Engineering, University of New Hampshire, Durham, NH. The goal of the measurements was to get experimental data in order to be able to evaluate the theoretical data received from the ray tracing during the theoretical investigation.

The idea was to shoot a laser beam through a water surface and capture the transmitted footprint below the surface using an under water camera. The

laser used was a continuous 30 mW 532 nm laser and the beam was given a divergence of 33 mrad with the use of a divergent lens. The laser was placed 4.14 m above the water surface and since the Hawk Eye II system operates with a nadir angle of 20 degrees this nadir angle was chosen here as well. This setup gave us a footprint with a Gaussian cross-section and a diameter, at the water surface, of 138 mm measured with the $1/e^2$ convention.

Beneath the surface a frosted sheet of plastic was placed and tilted 15 degrees making it normal to the light propagation if the water surface was flat. The propagated laser beam illuminated the sheet and the footprint could be seen from the back side of the sheet. By using an under-water camera to take still photos from the back side, at a rate of 1 Hz, snapshots of the footprint were captured. Each single snapshot is to represent the result of one laser pulse intersecting a static water surface. From the images one could then extract intensity profiles giving us similar information about new directions of the beam as from the theoretical investigation described earlier. Figure 4.3 illustrates the setup.

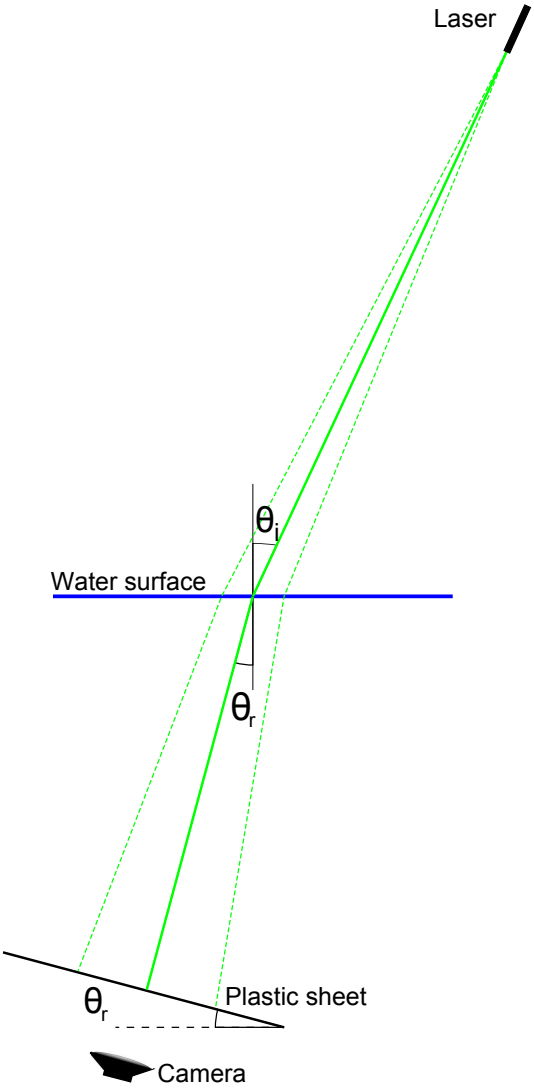

Figure 4.3: The setup in the wave tank.

The footprint will have different shapes depending on what depth it is captured due to wave focusing. The photographs were captured at a depth of 1.7 m. From the intensity profiles the center of intensity will be calculated for each photograph. From the position of the center, a direction deviation in comparison with the main direction for flat waters will be calculated.

With increasing water depth follows increasing accuracy for the measurements. The distance from the reference center position to the position of the distorted footprint will be measured. If the distance between the plastic sheet and the laser intersection point of the water surface is short, a small measuring error will cause a large error when calculating the deviation. If the distance is larger, the same measuring error, will give a smaller error when calculating the

deviation. The depth was determined by the depth of the wave tank were the experiment was conducted.

Waves on the air/water interface was produced by using a large fan placed just above the water surface at a distance of 4.25 m away from the intersection area. The fan provided a steady wind generating capillary and small gravity waves in the area of interest.

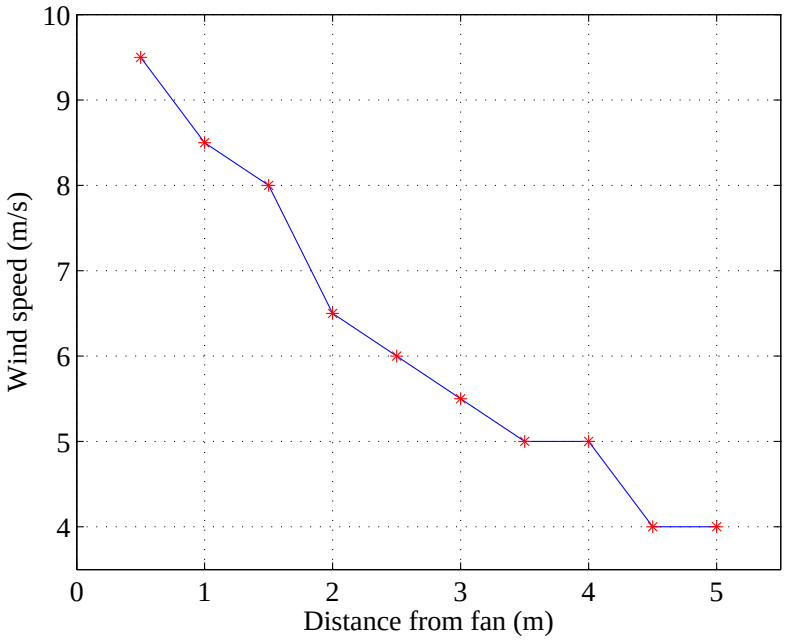

Figure 4.4: The wind speed measured over a distance of 5 m from the fan

The amplitude of the waves was measured using a staff meter providing a voltage proportional to the wave height. By sampling the wave amplitude with a rate of 200 Hz a time series of the wave elevation is received. From this data, the present wave spectrum was calculated by doing a Fourier Transform. This spectrum will be used later when creating surface structures used in o theoretical investigations. Gathering information about the angular spreading requires additional instruments. Instruments that were not available at the time. Instead, basic angular spreading models will be used and the obtained surfaces will be compared with photographs taken of the real waves to verify the results from the model. Nevertheless, this obviously this introduces uncertainties.

In this way, light direction measurements from an air/water interface were the wave spectrum of the surface to a large extent is empirically known, will be available. This will be valuable information when verifying the simulations.

Chapter 5

Generating 3D surfaces

Generating realistic ocean surfaces has been an important topic in computer graphics for a long time e.g. for the game industry or the movie industry. The method of using a spectral approach was first presented by Mastin et al. 1987[18] but originates from earlier work[5]. It is considered one of the best methods of generating realistic ocean waves and has been used to simulate the ocean for example in the movies *Titanic* and *Waterworld*[5]. One downside has been the extensive use of computer power needed in comparison with other methods.

5.1 Random Complex Spectrum Method

By assuming that the surface consists of plane waves having different frequencies, amplitudes and phases as explained in 3.2, a surface can mathematically be described by Equation 5.1

$$h(\boldsymbol{x}, t) = \sum_{\boldsymbol{k}} \tilde{h}(\boldsymbol{k}, t)(\cos(\boldsymbol{k} \cdot \boldsymbol{x}) + i \sin(\boldsymbol{k} \cdot \boldsymbol{x})) \tag{5.1}$$

where $h(\boldsymbol{x}, t)$ is the elevation in the spatial domain at location $\boldsymbol{x}$ and time t. $\tilde{h}(\boldsymbol{k}, t)$ is the complex fourier amplitude in the frequency domain at time t for the angular wavenumber $\boldsymbol{k}$.

$\boldsymbol{k}$ is the angular wavenumber in two dimensions defined as $\boldsymbol{k} = (k_x, k_y)$. The values of k_x and k_y are dependent on how large one wants the spatial domain to be and what resolution one wants to achieve. A spatial domain, also called patch, with sides L_x and L_y and a grid with N respectively M points at each side will have angular wavevectors according to $\boldsymbol{k} = (k_x, k_y) = 2\pi(n/L_x, m/L_y)$. The integers n and m are limited to $-N/2 \leq n < N/2$ and $-M/2 \leq m < M/2$. Higher values of M and N gives better resolution but increasing computational time. There will be a trade off between the smallest necessary resolution depending on patch size and number of grid points. Figure 5.1 shows a small example of a spatial domain and the real part of the frequency domain on a 16 by 16 grid.

The key step in the process when creating a realistic surface is to define the complex Fourier amplitudes in the frequency domain according to the statistics of a wavespectrum and then use Fourier Transform to get the corresponding spatial domain. The method used is called *Random Complex Spectrum Method*[19].

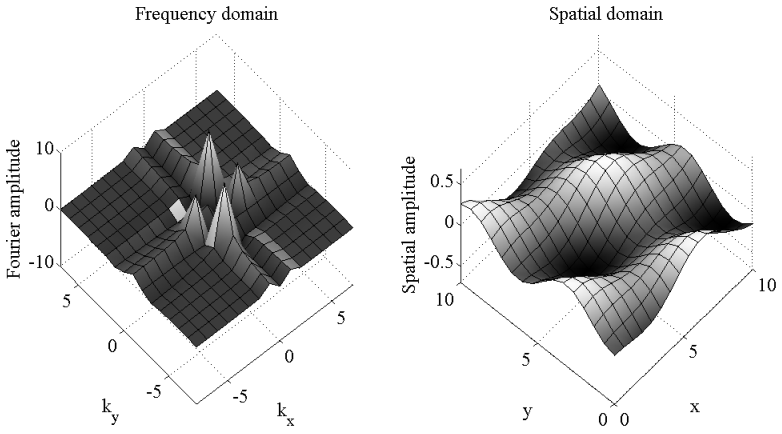

Figure 5.1: Real part of the frequency domain with 16x16 points and corresponding spatial domain with each side at 10 m.

Since the wave spectrum models presented earlier are continuous but discrete points are needed for the calculations a conversion like in Figure 5.2 needs to be done. The total amount of energy should not change so the calculations have to adjust for that. This is done by multiplying each discrete value with Δk_x if the spectrum is one dimensional and by $\Delta k_x \Delta k_y$ if the spectrum is two-dimensional where

$$\Delta k_x = k_{x_{n+1}} - k_{x_n} = 2\pi / L_x$$

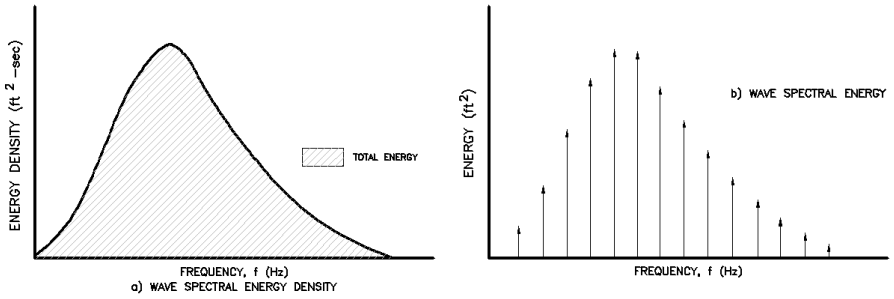

Figure 5.2: General continuous wave spectrum and the same spectrum represented by discrete frequencies.[10].

For each two-dimensional wavenumber, a random complex Fourier coefficient $\tilde{h}(\boldsymbol{k}_i) = A_i + iB_i$ will be generated. A and B are chosen using

$$A_i = \xi_{i_{re}} \cdot \sqrt{S(\boldsymbol{k}_i)/2} \tag{5.2}$$

$$B_i = \xi_{i_{im}} \cdot \sqrt{S(\boldsymbol{k}_i)/2} \tag{5.3}$$

where $\xi_{i_{re}}$ and $\xi_{i_{im}}$ are real Gaussian distributed random variables with mean at zero and a standard deviation of one. S is the wave spectrum of the surface to simulate. It can origin from a measurement or from a wave spectrum model. The final relation for how to produce an initial spectral domain will be

$$h_0(\boldsymbol{k}) = (\xi_{i_{re}} + i\xi_{i_{im}}) \cdot \sqrt{S(\boldsymbol{k})/2} \tag{5.4}$$

$$h_0(-\boldsymbol{k}) = (\xi_{j_{re}} + i\xi_{j_{im}}) \cdot \sqrt{S(-\boldsymbol{k})/2} \tag{5.5}$$

Here it is important how the wave spectrum $S(\boldsymbol{k})$ is defined. If it is symmetric i.e. $S(\boldsymbol{k}) = S(-\boldsymbol{k})$ it will result in a surface consisting of waves traveling parallel as well as against the wind. However in most cases for a wind driven sea a majority of the waves are traveling parallel to the wind or in nearby directions. Waves propagating perpendicular and even against the wind are present but only to a small extent. These properties are defined in the angular spreading function described in Section 3.3. In this case the angular spreading function does not make a distinction between two waves traveling in opposite direction. It only specifies that the amount of energy for that frequency in those two directions. Taking a double sided spectrum and simply setting the "backward traveling" part of the spectrum to zero is not correct since this will violate the total amount of energy in the spectrum giving misleading results.

Figure 5.3 shows an example of the PM-spectrum expressed as a one-sided spectrum respective a two-sided spectrum. The case gets simpler if one assumes that no waves have a propagation component against the wind or propagates perfectly perpendicular to the wind. Then the left side of the spectrum can be put to zero and the positive side multiplied with two to preserve the same amount of energy in the spectrum. However in this case another method, described below, will be used.

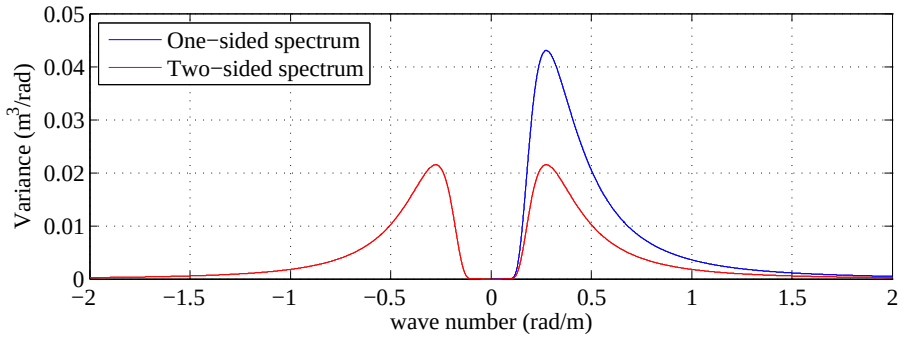

Figure 5.3: Phillips spectrum expressed in a one-sided respective two-sided spectrum..

The surface one wants to generate has a real surface elevation and therefore a complex output from the Fourier transform would not make any sense. To receive a purely real output a so called a hermitian Fourier Transform[19] is needed. The criteria on the coefficients is

$$C_{N+i} = C^*_{N-i+1} \tag{5.6}$$

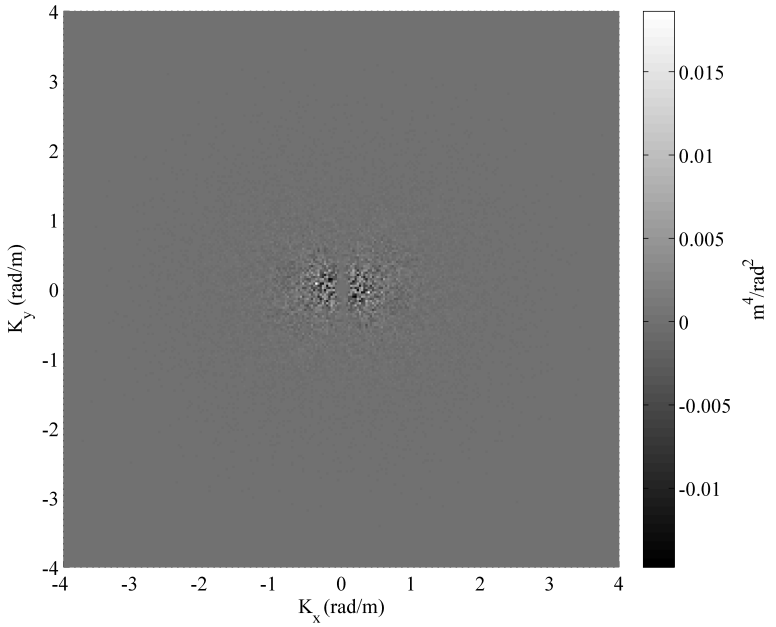

Figure 5.4: Example of generated Fourier coefficients in spectral domain

Tessendorf[5] presented a way to achieve this and at the same time making us able to move the waves in time. At the same time it also sets the direction of the waves. Starting of with the one sided spectrum with the part containing components against the wind to zero and using Equation 5.7

$$h(\boldsymbol{k}, t) = h_0(\boldsymbol{k})e^{i\omega(k)t} + h_0^*(-\boldsymbol{k})e^{-i\omega(k)t} \tag{5.7}$$

$$h(-\boldsymbol{k}, t) = h^*(\boldsymbol{k}, t) \tag{5.8}$$

gives us coefficients as in 5.8 corresponding to the criteria in relation 5.6. t is the time which is arbitrary and $\omega(k) = \sqrt{gk}$ is the angular frequency as in Equation 3.9. Because of this operation the amount of energy in the spectrum will be doubled and therefore no multiplication with two should be done.

This is the final wave spectral domain which will be transformed into the spatial domain. Figure 5.4 shows an example of the real part of a spectral domain. The ECKV model was used and Figure 5.4 should be compared with Figure 3.9 where the spectral components not yet have been multiplied with a random constant.

5.2 Implementing the spectrum

A Fast Fourier Transform algorithm was used for the transformation from the spectral domain to the spatial domain. Depending on used algorithm different adjustments of the spectrum needs to be done before applying the FFT. NVIDIA's CUFFT library was used in order to make use of the parallel computation capability in NVIDIA's graphical cards[20].

As in many other FFT algorithms the frequency domain is not centered around the DC component but instead around the Nyquist frequency. Therefore the used spectrum needs to be shifted meeting those criterias. The shifting is done by dividing the domain in four equally large sections and transfer their locations diagonally. One very important impact from this is that high wave numbers are now situated in the center of the domain. Figure 5.5 illustrates the difference between a shifted and an unshifted spectrum for a small grid with eight by eight elements. The row and the column were either one of the x or y component is zero are encapsulated by the blue rectangles.

Unshifted

11	12	13	14	15	16	17	18
21	22	23	24	25	26	27	28
31	32	33	34	35	36	37	38
41	42	43	44	45	46	47	48
51	52	53	54	55	56	57	58
61	62	63	64	65	66	67	68
71	72	73	74	75	76	77	78
81	82	83	84	85	86	87	88

Shifted

55	56	57	58	51	52	53	54
65	66	67	68	61	62	63	64
75	76	77	78	71	72	73	74
85	86	87	88	81	82	83	84
15	16	17	18	11	12	13	14
25	26	27	28	21	22	23	24
35	36	37	38	31	32	33	34
45	46	47	48	41	42	43	44

Figure 5.5: Unshifted spectrum layout and shifted spectrum layout.

5.3 How to decide range and resolution of the spectrum

When setting the dimensions for the spectrum, the wanted spatial resolution needs to be decided. Due to surface tension the amount of extremely small facets in water disturbed by moderate winds are limited. Arnott states that the wavelength of the small ripples created by a calm wind over a flat surface has a wave length around a few centimeters[6]. Higher wind speeds will generate larger waves but it is also reasonable to assume that higher wind speeds will generate waves of shorter wave lengths at the same time. In this study the distance between two grid points will therefore be set to 5 mm. Going below that is of no use since linear theory starts to be a bad approximation for those wavelengths. This grid distance in combination with the size of the largest

waves present at the location will give us the total number of points needed in the spectrum. Explanation is done by the the use of an example. Lets say that according to the wind and fetch conditions, the largest wave one need to be able to simulate is 20 m. Therefore must the patch have the side of 20 m. Also, if the wanted grid distance is 5 mm one needs 4000 grid points along each side of the patch. In total that would mean 16 millions grid points in both the spatial and spectral domain. Since the FFT algorithm needs a grid point number as a multiple of two to be efficient 4096 points on each side would be the natural choice. How large the patch needs to be is described earlier in Section 4.1.

5.4 Generating a TIN model

When conducting the Inverse Fourier Transform on the spectrum one will receive the surface elevation for each grid point. This is however not enough when conducting the ray tracing. Instead one is mainly interested about the slope of the surface. By connecting grid points to each other using triangles a triangulated irregular network (TIN) will be constructed. Each triangle facet will have a slope and a surface normal useful when conducting the raytracing. Figure 5.6 shows an example of a coarse TIN constructed explained above.

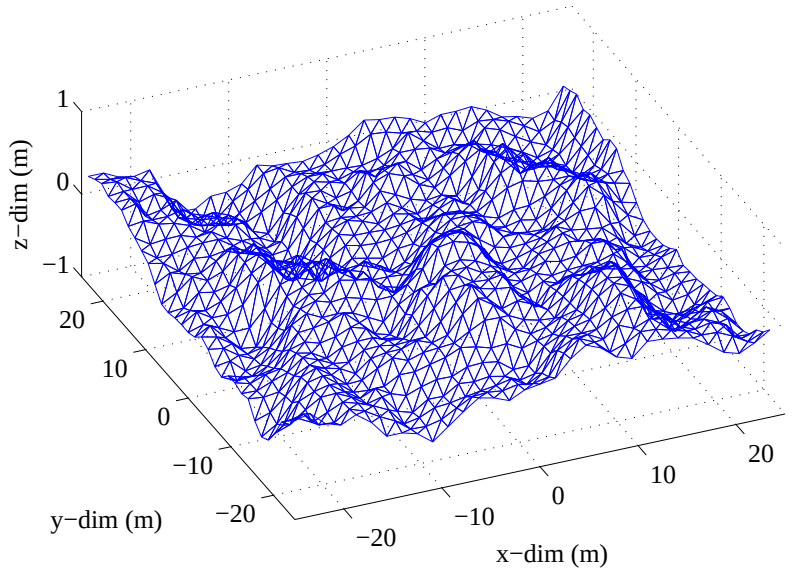

Figure 5.6: A generated coarse surface sample with the triangle mesh ploted in MatLab .

The resolution in the example is not by far good enough for this study and can only visualize the shape on the large scale. Figure 5.7 shows a rendered example of a TIN with much higher resolution. The surface is ten by ten meters with a grid resolution of 1 cm. For rendering, the open source rendering software,

Blender, was used. Since the program uses the same technique as the simulation code it gives a hint of how realistic the surfaces are.

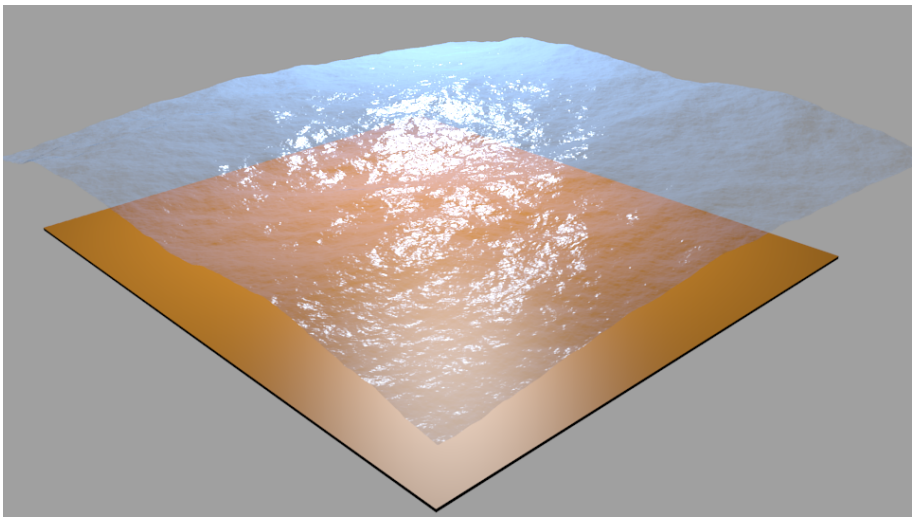

Figure 5.7: A generated surface sample with high resolution rendered in a Blender.

5.5 Verifying the surface structure

Just looking at the surface is not good enough when examining if the surface is realistic or not. Instead methods to quantify the wave parameters for the waves and compare them with real waves is needed. One way of doing so is to look at the significant wave height, H_S. The significant wave height has been and is one of the most common ways to describe the sea state. Originally it is defined as the average height of the highest one third of the waves. The reason for this somewhat strange definition is that it had good agreement with how an experienced sailor would describe the sea state[10]. The new definition uses the standard deviation of the surface elevation, σ_η and is defined as

$$H_S = 4\sigma_\eta$$

One can also calculate the significant wave height by the use of the wave spectrum. Integrating over the entire spectrum and multiply the square root of the result by four gives the significant wave height-

$$H_S = 4\sqrt{m_0} \qquad \text{where} \qquad m_0 = \int_0^\infty E(f)df$$

By generating surfaces for different wind conditions and compare the significant wave height with the values stated in the Beaufort scale one can evaluate the surfaces. The result is presented in Figure 5.8

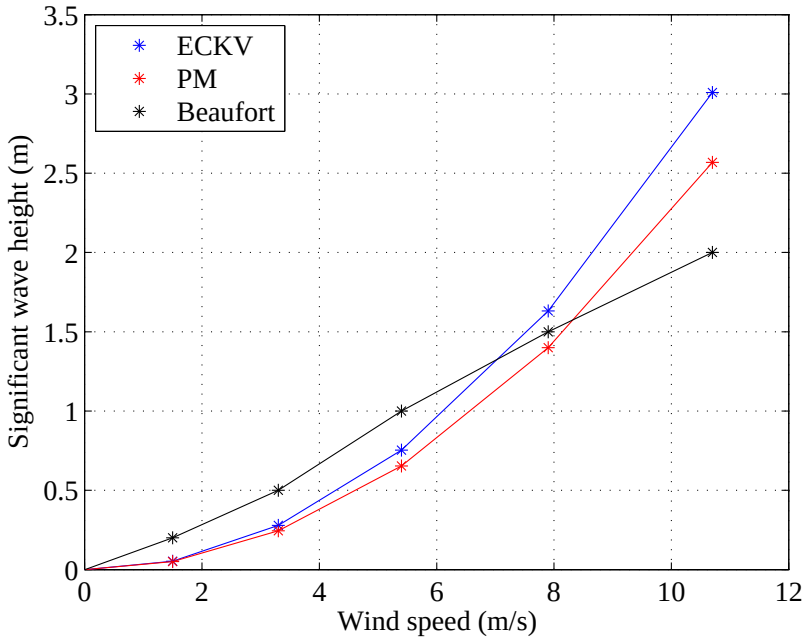

Figure 5.8: Significant wave heights calculated from the ECKV spectrum and PM spectrum. They arecompared with the wave heights as stated in the Beaufort scale.

Both spectrum models estimates the significant wave height a bit lower than what is stated in the Beaufort scale when low wind speeds are considered. This might indicate that the constructed surfaces are less disturbed than what would be correct. On this point one have to rely on the inventors of each spectrum model that their models are based on a solid foundation. Other spectrum models might give different results.

Chapter 6

Measurements and Simulations

6.1 Experimental approach

6.1.1 Shading model

The amount of light falling into a camera from an area within the field of view is dependent on several aspects. The most important aspect is of course the amount of light emitted from the particular area. Another aspect, less obvious but nevertheless very important in this experiment is were the area is located in respect to the camera. Figure 6.1 shows a light source extending over a plane with the camera mounted beneath it facing along the normal to the plane.

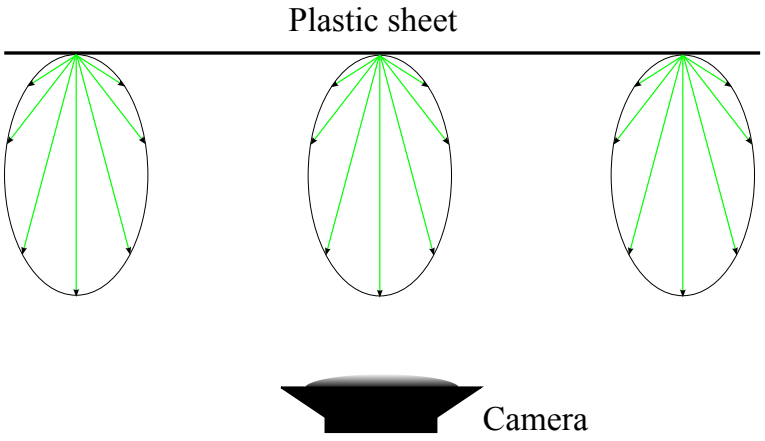

Figure 6.1: Different amount of light is detected by the camera due to shadowing effects in the camera lens system.

Even though the same amount of light is emitted from different parts of the plane, the difference in direction towards the camera causes the received amount of light to differ. The reason is called the shading effect and is due to properties

of the lens system. Some light coming from the outer parts of the plastic sheet is internally blocked by the lens system because of difficulties when compensating for aberration. This is a problem since the amount of light captured within the images will be used as a measurement of the amount of light on the frosted sheet. To solve this problem a shading model was constructed.

To construct the model, ten images not illuminated by any laser light was used. From those images, the values from the green channel was extracted into a matrix with the same dimensions as the pixel dimensions of the images. The values from each pixel of all ten images was summed and then divided by the number of images giving an averaged image-matrix. The image-matrix was then cropped into 1615x1615 elements making sure that it is only covering the area of interest.

Then the averaged image-matrix was filtered by using the MatLab function *filter2*. The function had two input parameters and performed a smoothing of the data by doing a 2-dimensional correlation[22]. The first argument was the Finite Impulse Response filter. The size of this filter defined the amount of smoothing. Larger sizes yield more smoothing. In this case a 15 by 15 matrix was chosen. The sum of the elements in the filter should be 1. The second argument into the function was the image-matrix.

What *filter2* does is that it places the filter-matrix over the image-matrix with one of the image-elements of interest in the middle. Then the elements of the filter matrix was multiplied with the corresponding image-matrix element. Thereafter the sum of those multiplications were calculated yielding a result value for this particular element in the image-matrix. This procedure is repeated for each and every element in the image. After the use of *filter2* the edges needed to be cropped since the edge elements are surrounded by empty values outside the image making the values misleading. The final result was a smoothened image-matrix representing an average image.

The next and final step of the model construction was to find the maximum value of the image-matrix and divide every element with this value. This gave a matrix with positive values less than one, depending on the amount of light received from the corresponding area of the frosted sheet. This matrix is the shading model and the lowest value in this particular case was 0.79. Figure 6.2 shows the 2-dimensional shading model.

When analyzing an image, each element of the image was divided by the corresponding value from the shading model matrix. Pixels with a model value of one were unaffected while pixels with lower model values were increased. This will compensate for the differences caused by pure geometrical considerations.

The effects from the model is best illustrated by an example. A sample not illuminated by any laser light is chosen. One row of elements from the central part of the image is extracted, smoothed and visualized in Figure 6.3a. Then the same row of elements is compensated by the shading model before shown in Figure 6.3b. The difference is clearly seen on the shape of the curve. In the uncompensated plot the values are higher in the middle than at the edges. This is wrong since they are representing areas of the frosted sheet which are equally illuminated. In the compensated plot, the level has been adjusted giving us a realistic output.

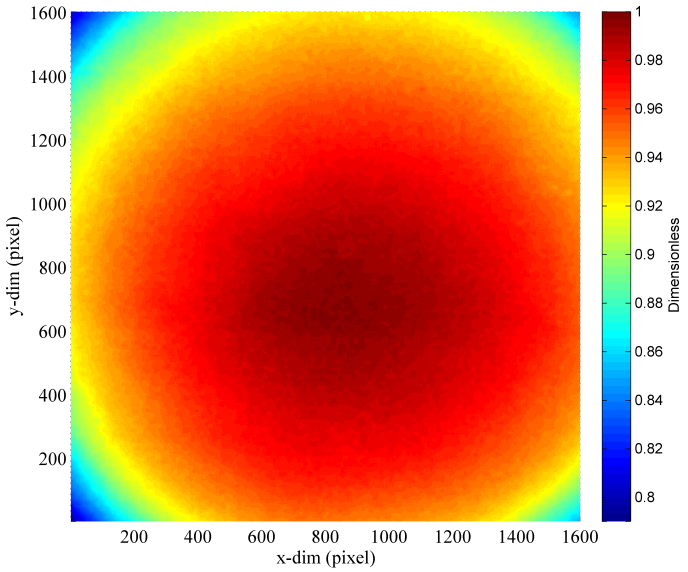

Figure 6.2: The 2-dimensional shading model representing each pixel with a positive value of one or smaller.

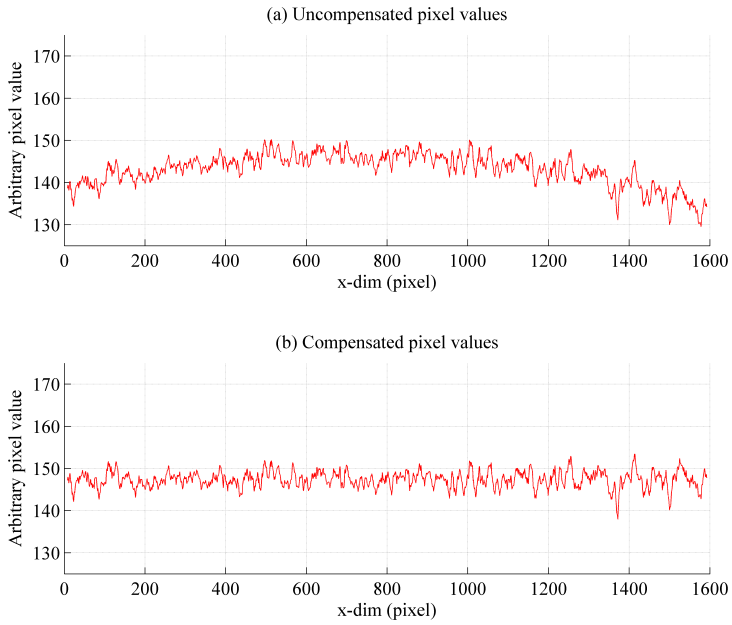

Figure 6.3: Example of the effects of the shading model. The same row of pixels was analyzed. (a) no shading model was used giving lower pixel values at the edges, (b) the shading model was used yielding that all pixels values are positioned around the same level.

6.1.2 Image analysis

The reason for analyzing the images on the frosted sheet was to get information about the directions of the refracted light. The idea is to use the intensity information in the images expressed in Cartesian coordinates to calculate the main traveling direction of the beam. By doing this for many images one will receive random draws from a distribution and those values can be used to estimate the distribution parameters. The results will be compared with the results from the simulations.

Preparing the images

The first step when analyzing an image, illuminated by laser light, is to prepare it by cropping it to the same dimensions as the shading model, previously explained, and to extract the green channel into a matrix. The next step is to divide each element of the image matrix by the corresponding shading-model element. Figure 6.4 shows an example.

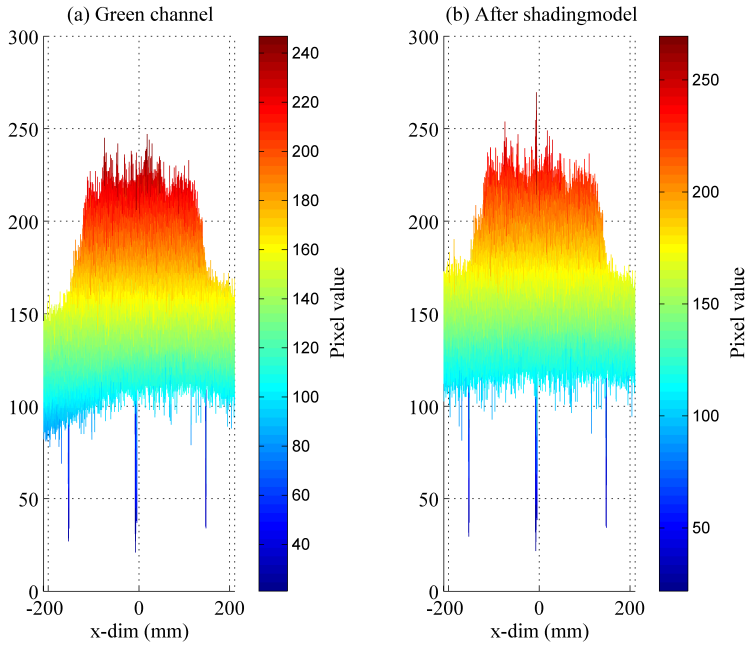

Figure 6.4: (a) An intensity profile extracted from an image without any modification. (b) The shading model have been applied. The sharp peaks in both images rises from marks on the plastic sheet.

Then, the same thing is done for a second image with no laser illumination. This information is needed to subtract the background noise. From the background-matrix, one calculates a number denoted ΔBG by taking the difference between the maximum and the minimum value and multiply it with a number slightly larger than one to get some extra margin. The extra margin

ensures that the largest difference in the noise will smaller than ΔBG. By testing different values, 1.2 appeared to be a good choice. ΔBG will be used to find a threshold in the analyzed images.

$$\Delta BG = 1.2 \cdot (max - min)$$

Finding the threshold is done by taking the minimum value in the image-matrix and then comparing every element value with the sum of the minimum value and ΔBG. Then, the median value and the standard deviation, σ_{BG}, of all the values smaller than this threshold were calculated. After that the median value was extracted from the element values in the entire image-matrix and every value smaller than σ_{BG} was set to zero. The procedure is explained by an example in Figure 6.5 where the shading model has already been applied.

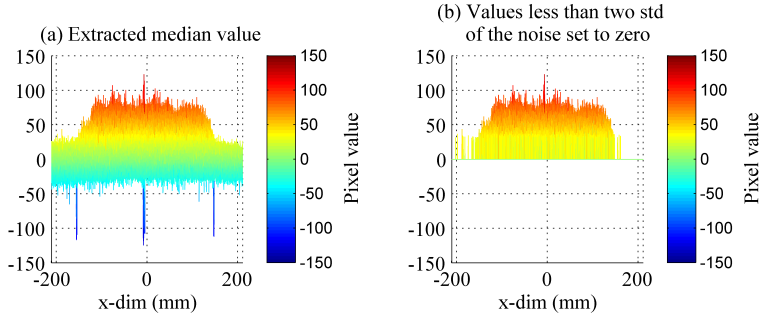

Figure 6.5: (a) The median value of the noise is extracted from all elements centering the background noise around zero. (b) Every element smaller than the sum of ΔBG and the minimum value is set to zero.

Finally in the image preparation one combines many pixel elements into larger ones giving a more pixelated matrix but also a less noisy one. The information that is lost by doing so is negligible as long as the new pixels are not too few. If the new number of pixels are 160 x 160 it means that, in this set-up, each pixel represents slightly less than 0.1 degrees which is detailed enough for the task. Figure 6.6 shows the initial image and the information obtained after processing the information as described. This information will be used to find the main direction.

Calculating main direction

When calculating the main direction for each image, a technique identical to the one used when the center of gravity of a body is calculated in mechanics, will be used. Each pixel has a value between zero and 255 where zero means no light and 255 means saturation of the pixel. By regarding this value as a weight representing the amount of light for this pixel and using the pixel location, the moment of force can be calculated for each pixel. Calculating the center of gravity is then straight-forward by the use of Equation 6.1

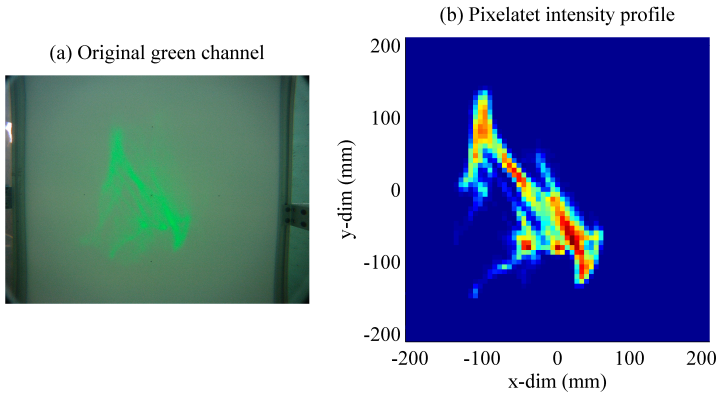

Figure 6.6: (a) The initial image. (b) The final image after applying the shading model, extracting background noise and pixelating the picture.

$$Center\ of\ gravity = \frac{\sum m_i \mathbf{r}_i}{\sum m_i} \tag{6.1}$$

where m_i, in this case, is the weight of pixel i and $\mathbf{r}_i$ is the vector to the pixel.

The same procedure was repeated for all images, and the location of the center was stored giving a set of data. Then, the parameters to a distribution corresponding to the data set was estimated. This distribution was the final result from the experimental part of the investigation.

The same investigation was done for ten images, captured when the water was flat, giving an undisturbed footprint on the sheet. This defines the reference direction which was compared with the expectation value in the direction distribution. Since those images were very similar to each other the variation between their main directions was very small.

6.1.3 The wave tank conditions

The fan placed over the water surface provided a wind as described in Figure 4.4. By using of a staff meter the elevation of the surface over time at a single point was measured. Figure 6.7 shows a sample of the profile of a one-second long time interval.

By using software developed by Dr. James Irish at the Center for Coastal and Ocean Mapping in Durham, New Hampshire, the frequency spectrum was computed describing the waves in the tank. Figure 6.8 shows this spectrum.

The largest peak is located at 4 Hz which is equivalent with a wavelength of 10 cm and a wave number of 64 rad/m. As one would expect, the peak frequency in this spectrum is higher than the peaks in the modeled spectra in Figure 4.1. The wind power in the experiment is not sufficient for building up large waves with lower frequencies. It can also be seen that the amount of energy is much smaller. Also the shape differs with two peaks in the wave tank spectrum instead of one.

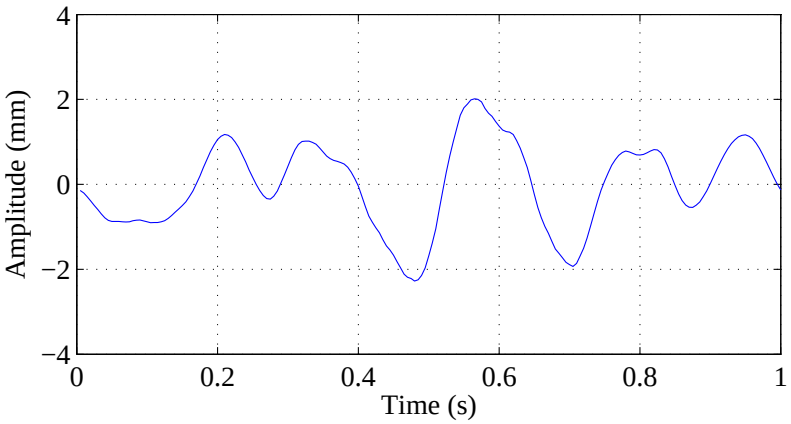

Figure 6.7: An example of the surface elevation in the wave tank as a function of time.

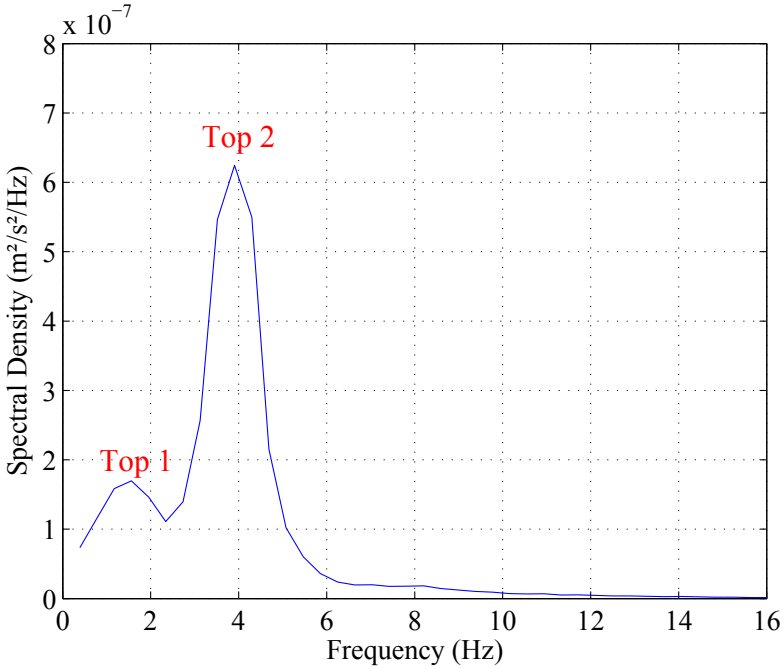

Figure 6.8: The measured frequency spectrum describing the waves produced by the fan in the wave tank.

6.2 Theoretical approach

6.2.1 Surface dimensions for ray tracing

Generating a surface able to describe waves up to 20 m with a resolution of 5 mm results in a surface consisting of 33.5 million triangles. Tracing millions of ray through a surface like that is very time consuming and one should reduce this if possible. Therefore, an investigation of how big surface one needs in order to trace the vast majority of the photons, was done.

The laser beam of an operating Hawk Eye 2 system has a divergence of 14 mrad giving a beam radius of 2.24 m after propagating a distance of 320 m. From this, an intensity profile of the light can be calculated and expressed as in Equation 6.2

$$I(r) = I_0 e^{-\frac{r^2}{2\sigma^2}} \tag{6.2}$$

where r is the distance from the center of the beam. Given $I(r = 2.24) = I_0/e^2$ it is found that σ is 1.12 m. Since Equation 6.2 expresses the light distribution at the water surface one can calculate how large amount of the energy that is received for different horizontal extensions of the water surface. The amount of energy, E, striking a surface of radius, R, is calculated by using Equation 6.3.

$$E(R) = E_0 \int_0^R \int_0^{2\pi} e^{-\frac{r^2}{2\sigma^2}} r dr d\varphi =$$

$$2\pi E_0 \int_0^R e^{-\frac{r^2}{2\sigma^2}} r dr = 2\pi E_0 \sigma^2 \left(1 - e^{-\frac{R^2}{2\sigma^2}} \right) \tag{6.3}$$

The total amount of energy received by a surface with infinite radius is given by $E_{tot} = E(\infty) = 2\pi E_0 \sigma^2$. For a radius of 2.24 m one obtains, $E(2.24) = E_{tot} \cdot 0.865$ which is expected. Searching a minimum radius within which almost all light is striking the surface shows that for a radius of 4 m 99.8 percent of the energy is received. Therefore this is selected as the minimum surface size. In order to represent the big waves one still needs to create a surface patch of 20 x 20 m but before conducting the ray trace, a patch of 8 x 8 m can be cut out. The number of triangles is now down to 5.4 millions.

Similar reasoning gives the minimum surface when recreating the setup in the wave tank. A beam radius of 6.9 cm after 4.2 m propagation gives a σ of 0.0345 m. 99.8 percent of all energy will strike the water surface if it has a radius of 12.3 cm.

6.2.2 Simulation conditions

Before conducting the simulations one needs to decide under which conditions they should be performed. Dependence of wind speed is of course important and therefore one investigation was to conduct simulations with varying wind speeds while keeping all other parameters fixed. This investigation was conducted twice with the only difference that the laser direction had changed 90 degrees in comparison to the wind. First the laser was traveling with one component in the positive x-direction and none in the y-direction. After that, the component

in x-direction was set to zero and the y-direction component was given the same value as the x-component had before. The nadir angle always remained at 20 degrees and the wind was always blowing in the positive x-direction. The chosen wind speeds was 3, 4 and 5 m/s respectively. Figure 6.9 shows the schematic difference between the two set-ups.

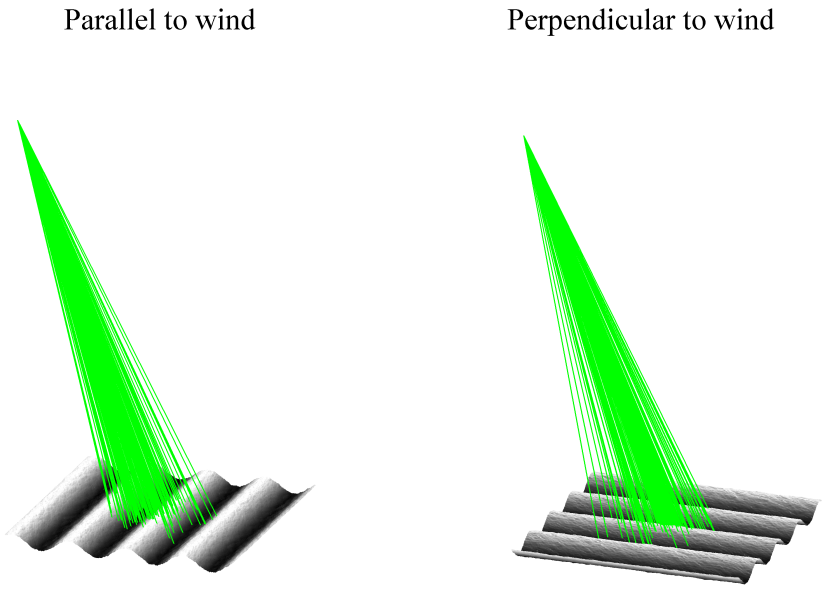

Figure 6.9: The two setups schematically presented. In the first one the laser beam had a horizontal component parallel to the wind. In the second the horizontal component was perpendicular to the wind.

Another interesting parameter is the fetch size and therefore one investigation only varying this parameter was conducted. Chosen wind speed was 3.5 m/s because then surfaces could be generated even when the sea is fully developed, without creating waves larger than a patch size of 20 x 20 m as explained in Section 5.3 and 4.1. Chosen fetch sizes were 10, 25, 50, 100, 250 and 500 km, respectively. The spectra for those conditions was presented earlier in Figure 4.1. In this case, the laser beam and the wind had parallel components.

One investigation was also conducted where the divergence of the laser beam was changed and thereby also the footprint on the water surface. In this study, the patch size was increased to 40 x 40 m. The reason for this was that it would make us able to generate surfaces describing a fully developed sea at 5.4 m/s which is the maximum wind speed before wave breaking occurs. Then one can compare the results with the error estimated by Guenther mentioned in Section 2.2.1. Because of this the resolution had to become coarser. The chosen surface diameters were 0, 0.5, 1.5, 2.5, 3.5 and 4.5 m, respectively.

Finally, one investigation where the surface was generated from the measured wave spectrum in the wave tank, was conducted. The parameters of the laser

were set according to tat experiment. The laser light was in this case traveling with a positive y component and no x component making it travel perpendicular to the wind.

One problem, when constructing the waves was that only information from one single point was available, i.e. no angular distribution information. One could have used the angular spreading function from the ECKV model described in Section 3.4.2 but this model is for waters affected by natural winds and not small fetches produced by a fan. Instead a modification of Equation 3.4 was chosen making it more directed without breaking the conditions from Equation 3.7. The new version was

$$\Phi(\varphi) = \frac{3.2}{\pi}\cos(\varphi)^6, \qquad |\varphi| < \frac{\pi}{2} \tag{6.4}$$

The reason for using this variant of the spreading function was that the generated surfaces had good agreement, along the direction perpendicular to the wind, with the photographs of the water surfaces. One has to admit that this method is very bulky but since no other information about the surface along this direction was available, this was the best attempt. When examining the final results one can evaluate whether it was a good choice or not. Table 6.1 summarizes the input parameters for the simulations.

6.2.3 Choosing the number of photons to simulate

The number of simulated photons is, together with the number of triangles in the surface, the main parameter affecting the computing time consumption. Therefore this number, just like the ray traced surface, also needs to be chosen with care. The number of photons should be sufficient not to violate the statistics of the data but an exceeding number is not necessary.

To find out what this number is a series of laser pulse simulations were conducted. To start with, several similar simulations over the same surface using a fairly low amount of photons was done. After calculating the mean direction for every pulse the variability of the mean directions was calculated. After this, the same investigation was performed on the same surface but with a larger number of photons in each pulse. By studying how the variability decreases with increasing number of photons one will get insight of how many photons that are needed. To be certain, this procedure was conducted on several different surfaces to see the statistics of the variation. Figure 6.10 shows the result of these investigations for three different surfaces.

For the investigation to be useful one also needs to specify when the variability can be considered sufficiently low, which is dependent on the accuracy we require in the results. This should be based on the accuracy needed when conducting ALB surveys. At a depth of 10 m a horizontal error of one centimeter corresponds to an angle deviation of 0.06 degrees which indeed is a high accuracy under those circumstances. This says that the pulse mean directions shall not deviate more than 0.06 degrees i.e. 95 percent of the pulses should be confined within those limits.

Therefore, a resolution not lower than 0.06 degrees, is needed from the results. If the standard deviation of the mean directions is 0.03 degrees then the statistical fluctuations will cause less than 5 percent of the pulses to deviate more than one centimeter. This is the maximum standard deviation that can

Table 6.1: The parameters for each investigation. $\parallel$ and $\perp$ indicaties if the horizontal component of the laser light is parallel respective perpendicular to the wind direction.

Wind speed (m/s)	**Fetch size** (km)	**Beam radius** (m)	**Laser altitude** (m)	**Direction to wind**
0	35	4.5	300	$\parallel$
3	35	4.5	300	$\parallel$
4	35	4.5	300	$\parallel$
5	35	4.5	300	$\parallel$
0	35	4.5	300	$\perp$
3	35	4.5	300	$\perp$
4	35	4.5	300	$\perp$
5	35	4.5	300	$\perp$
3.5	**10**	4.5	300	$\parallel$
3.5	**25**	4.5	300	$\parallel$
3.5	**50**	4.5	300	$\parallel$
3.5	**100**	4.5	300	$\parallel$
3.5	**250**	4.5	300	$\parallel$
3.5	**500**	4.5	300	$\parallel$
5.4	10000	**0.0**	300	$\parallel$
5.4	10000	**0.5**	300	$\parallel$
5.4	10000	**1.5**	300	$\parallel$
5.4	10000	**2.5**	300	$\parallel$
5.4	10000	**3.5**	300	$\parallel$
5.4	10000	**4.5**	300	$\parallel$
Fan	0.005	**0.069**	4.14	$\perp$

be allowed. However, one should also add a margin of safety. Therefore the number of photons was set high enough to give a standard deviation of 0.018 degrees and a resolution of 0.035 degrees. This is better than necessary but since only 15 000 photons are needed to achieve this accuracy, wouldn't add any significant computational time.

6.2.4 Preparing the result files

The result files were constructed so that each launched photon is represented by twelve floating point numbers and one integer. The twelve floating numbers represent the x-, y- and z-coordinates of the water surface intersection, the x-, y- and z-coordinates of the sea floor intersection at a specified depth, the cosine directions of the photon before impinging the water surface and the cosine directions after entering the water surface. The integer is a flag used for indicating

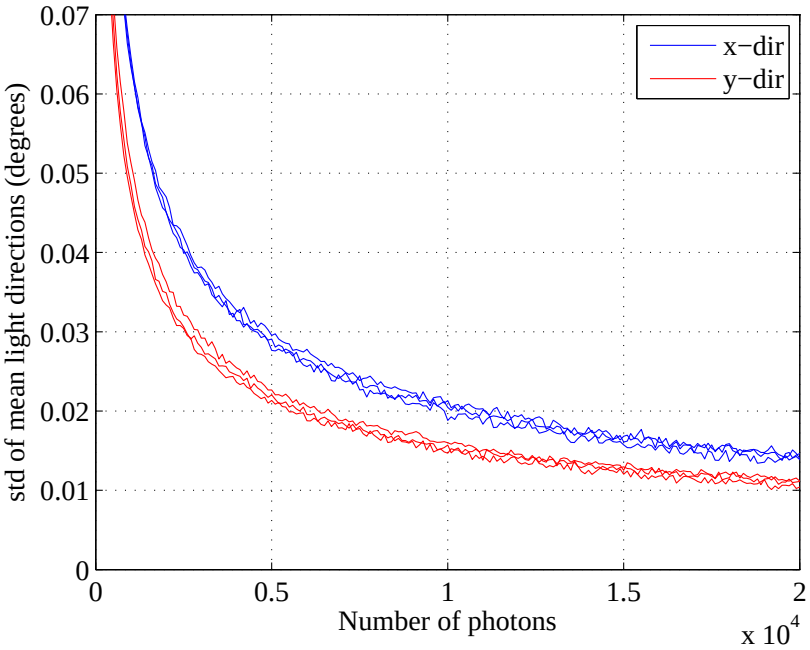

Figure 6.10: The variability of the mean light direction for each pulse is affected by the number of photons in each pulse. The six curves show the variability in x- and y-directions as a function of simulated photons for three different surfaces.

if the photon missed the entire surface structure.

With this coordinate information, intensity images can be created representing what would be seen by an underwater camera taking pictures of the refracted laser pulse. The intensity images will be similar to those from the experimental approach and are analyzed in a similar way. However, the main purpose with the entire project is to study the change in direction of the laser pulse. Unlike the experimental approach, the theoretical study gives direct information about those directions.

The direction information is expressed in direction cosine with the $\boldsymbol{z}$-axis pointing straight up, the $\boldsymbol{x}$-axis pointing along the direction of the wind and the $\boldsymbol{y}$-axis perpendicular to both the $\boldsymbol{x}$-axis and the $\boldsymbol{z}$-axis.

When visualizing the direction results, a tilted Cartesian coordinate system was chosen. In the new system, denoted S', $\boldsymbol{y}'$ is pointing in the same direction as $\boldsymbol{y}$ and then the system is tilted by an angle θ_r around this axis. θ_r is the direction of a refracted ray with an incident angle of 20 degrees towards a perfectly flat surface. Using $n_{air} = 1.00029$ and $n_{water} = 1.33335$ yields $\theta_r = 14.9$ degrees. This causes the $\boldsymbol{z}'$-axis to be aligned with the direction of propagation for rays intersecting a flat surface and $\boldsymbol{x}'$ and $\boldsymbol{y}'$ will be both perpendicular to this. The reason for choosing $\boldsymbol{z}'$ as explained is that this direction is the light direction that is assumed in ALB surveys conducted today, even if the water surface is not flat. By converting the direction cosine for the photons in the

new coordinate system into angles measured from the $\boldsymbol{z}'$-axis the results will be presented as angle deviations from the today assumed result.

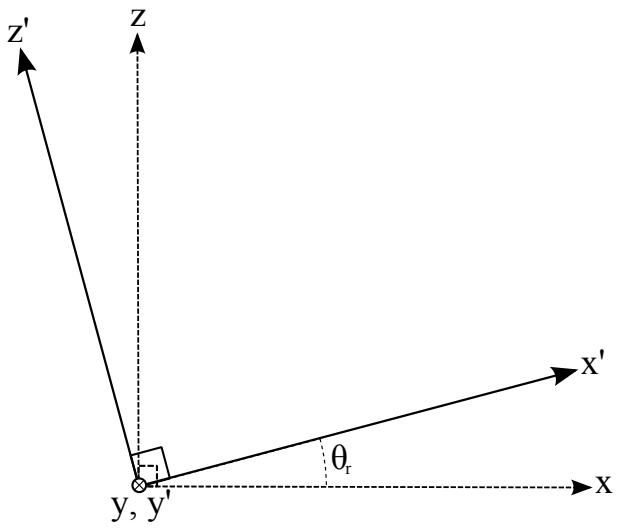

Figure 6.11: In the new coordinate system, the y′-axis is parallel to the y-axis but z′ and x′ deviate from their original axes by an angle θ_r

There are many other choices of coordinate systems that could be suitable. One major consideration when choosing this is that a direction deviation along the $\boldsymbol{x}'$-axis will be represented by an angle of exactly the same size as if the direction deviation would be along the $\boldsymbol{y}'$-axis. It means that the directions from a laser beam with a circular cross section will be presented in a direction plot as a circular pattern. The are many other coordinate systems were this is not the case. For example the pattern could instead be an elliptical or a skewed elliptical one. These representations would be not be wrong but maybe somewhat misleading.

6.2.5 Analyzing the result files

Each result file represents an individual pulse consisting of 15000 photons refracted through a unique water surface. The first step in the analysis is to transform the photon directions into the new coordinate system. Then the new x′-direction and the y′-direction are calculated for each photon. From those directions, the mean direction for all photons within that pulse can be calculated. The same step is repeated for every pulse in the simulation set. Figure 6.12 shows an example of one simulation set consisting of 2000 pulses where the mean direction for every pulse has been ploted.

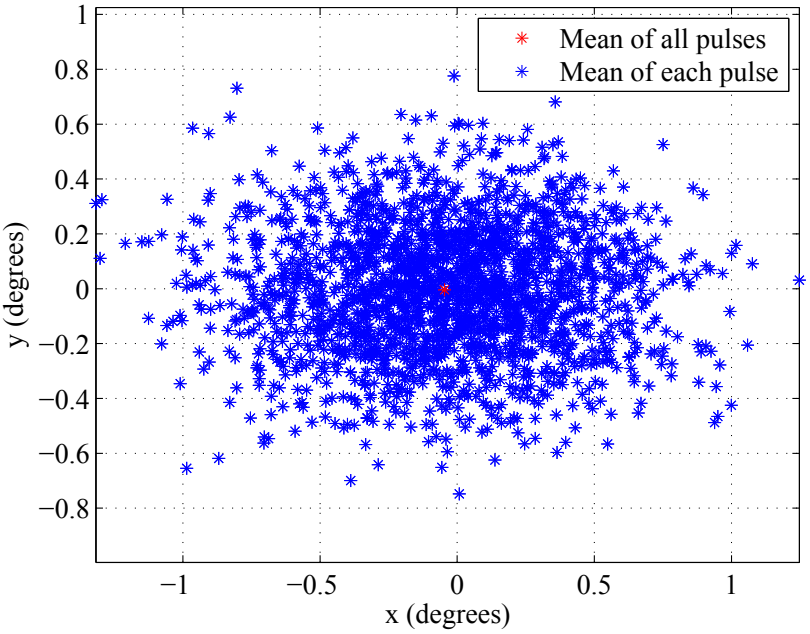

Figure 6.12: The mean directions for each pulse within a simulation set. The red dot is the average of all mean directions. In this example the wind speed was 4 m/s and the fetch size 35 km.

To this set of random draws, the distribution parameters are estimated making it possible to quantify the direction changes.

6.2.6 Seafloor illumination

To study the illumination ratio off an object, on the seafloor, the intensity profile of the footprint will be calculated for different water depths. In the IHO standards for bathymetric surveys, a 95 percent probability to detect an object of the size 2 x 2 m, is a criteria when conducting a survey of order 1a[21]. Therefore, squares of this size will be placed on the seafloor. Then the number of rays falling into the squares are counted. This number is compared with the total number of rays striking the seafloor. The procedure will be repeated for many pulses and for various water depths giving statistical data. From this data, the mean illumination ratio and the standard deviation will be calculated.

Figure 6.13 shows the two squares that were used in this study. The cross represents the point where the pulses were aimed at i.e. the point the rays would be centered around if the water was flat.

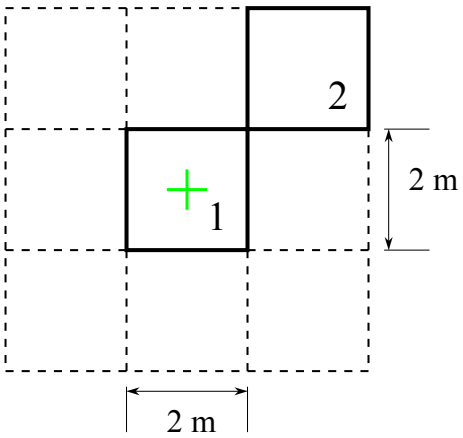

Figure 6.13: When studying the illumination ratio, two different square objects were chosen. Square 1 is located around the point to which the laser pulse was aimed at. Square 2 is centered around a point 2.8 m away.

Figure 6.14 shows an example of one pulse illuminating the seafloor at a water depth of 10 m. The two squares are marked by red lines.

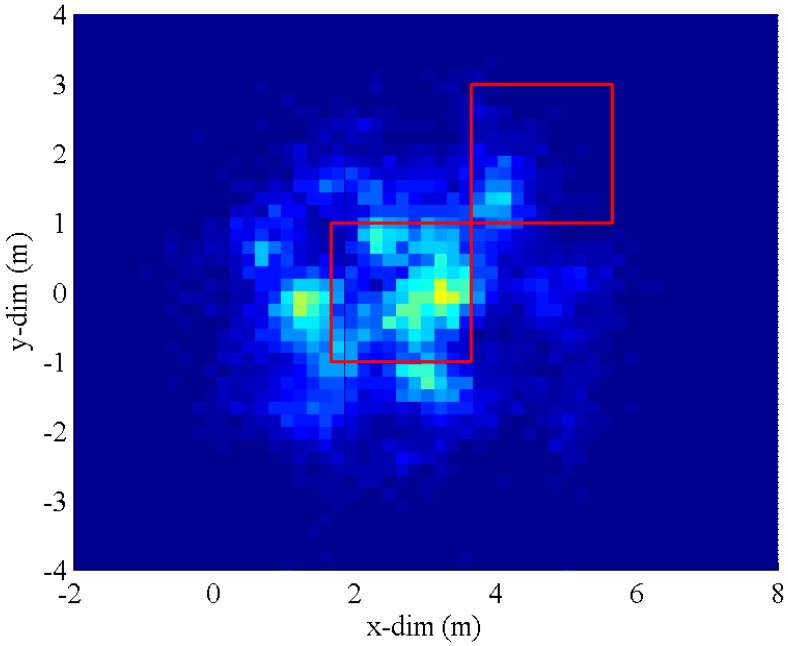

Figure 6.14: The illumination ratio of the two squares depend very much on how the shape of the footprint changes due to the water surface.

6.2.7 Simulating a photograph

When simulating the results from the wave tank one starts by doing a ray trace just like previously explained. From the result data, every photon is projected on to a plane representing the plastic sheet used in the wave tank. Then, the photons are gathered into simulated pixels to create an artificial image.

One needs to adjust the simulation results for how the information was extracted from the photographs taken in the wave tank. One big difference between the information of the two is that there is no background noise in the simulated results. As a consequence there is no information hidden in the noise. When analyzing the real images this information could not be extracted from the noise and was thrown away. Because of this the experimental result will have sharper intensity peaks. When calculating the variability of the mean direction this will be larger than expected since the low intensity parts, which have a smoothening effect, are not present.

Since one would like to compare apples with apples the simulated data needs to be adjusted accordingly. The simplest way of doing this is to first find the maximum pixel value. Then, decide a threshold as a ratio of the maximum value. When the information was extracted from the photographs the threshold was around 65 percent of the maximum value. Therefore this value will be used here as well. Every pixel value smaller than this was set to zero. The result is a less smoother intensity profile.

Chapter 7

Results and Discussion

The result after evaluating the directions from experimental or simulation data will be a two dimensional Gaussian distribution with varying parameter values. The parameter values are evaluated by applying the Matlab function *gmdistribution.fit*, from the statistical toolbox, yielding the estimated parameter values. The reason for using this function and not just *mean* or *std* is that one can specify the required tolerance with *gmdistribution.fit*. This gives a way to check if a Gaussian distribution is a good choice. It is important to point out that the probability distribution functions most likely are not perfectly described by Gaussian functions. Figure 7.1 shows two identical ray intersecting slopes with different angles.

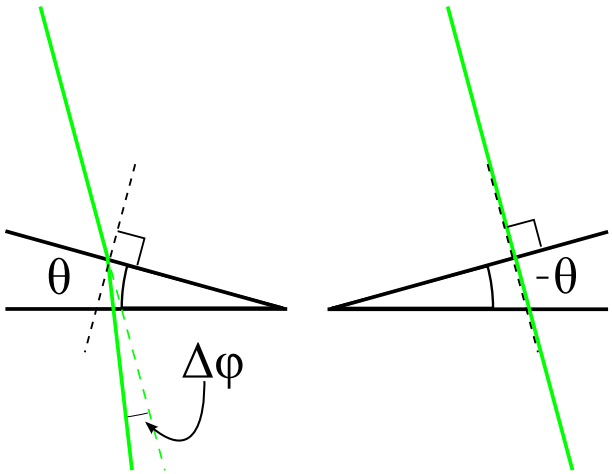

Figure 7.1: Two identical rays intersecting two different slopes.

A ray intersecting a facet with a positive slope of angle θ will be redirected by an angle deviation $\Delta\varphi$ as shown in Figure 7.1. The same ray striking a facet with a slope of angle $-\theta$ will not be redirected by an angle deviation of $-\Delta\varphi$. This is a consequence of Snell's law. The effect become larger when the nadir angle increases or if the surface becomes more disturbed.

For this study, were a 20-degree nadir angle is used and the waters are not too much disturbed the effect seams to be negligible. From this, the conclusion that a Gaussian approximation is justified, was made.

7.1 Real Ocean simulations

The changes between different simulations will be presented in tables and graphs. However, as a help when studying the results one example is presented in more detail. Figure 7.2 shows the approximated Gaussian distribution from a simulation were the wind speed was set to 5 m/s, the fetch size 35 km and the beam radius was 4.5 m. The wind direction and the horizontal direction component of the laser light were parallel to each other.

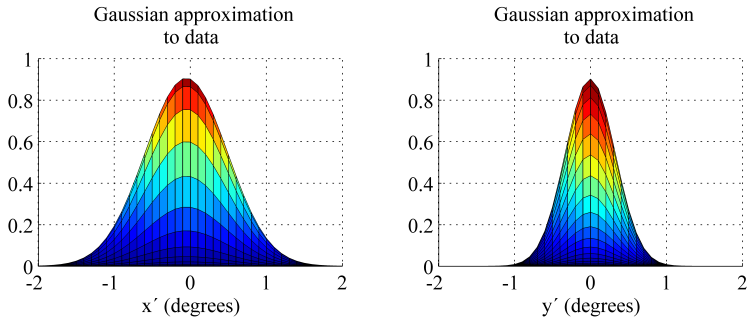

Figure 7.2: The calculated probability density function viewed from the y′-axis respective the x′-axis. The wind speed was 5 m/s and the fetch size was 35 km. The horizontal component of the laser light is parallel to the wind.

It is clearly seen that the light directions deviate more in one direction than in the other. This is expected since the waves traveling parallel to the the wind are larger than the ones traveling perpendicular causing the laser light to fluctuate more in one direction. In this particular case the deviation is almost twice as large in the x′-direction than in the y′-direction with a σ_x of 0.54 degrees and a σ_y of 0.33 degrees. A σ_x of 0.54 indicates that approximately 95 percent of the pulses are not expected to deviate more than 1.08 degrees in the x′-direction. In the y′-direction 95 percent of the pulses are expected to deviate less then 0.66 degrees.

When looking at the mean direction of all pulses one sees that the change is small in comparison with a flat surface. In the y′-direction the change is not seen at all. This is not strange since there are no parameters present that violates the symmetry of directions with respect of the x′-axis. However, this is not the case in the x′direction. This is due to the fact that a ray striking the surface closer to the airplane than the main laser direction will not be affected in the same way as a ray striking exactly the same surface but on the other side of the main laser direction. The incident angles will differ slightly. Most likely this is why one can see a tiny shift towards a smaller nadir angle than if the water would be flat. This might also indicate that the choice to approximate

with a Gaussian is less good in the x′-direction than in the y′-direction. The effect however, in this case, is so small that it can be neglected.

Table 7.1 shows the results from the investigations of the light direction deviation where the impact of the wind speed was studied. The results are also visualized in Figure 7.3. The blue line shows how the standard deviation of the mean light direction in the x′-direction changes and the red one shows the changes in the y'-direction.

Table 7.1: The parameters of the probability density function for different wind speeds. The fetch size is 35 km for all simulations. The horizontal component of the laser light is perpendicular to the wind.

Wind speed (m/s)	$\bar{x}$ (deg)	$\bar{y}$ (deg)	σ_x (deg)	σ_y (deg)
3	-0.02	0.00	0.22	0.12
4	-0.05	0.00	0.40	0.23
5	-0.05	0.00	0.54	0.33

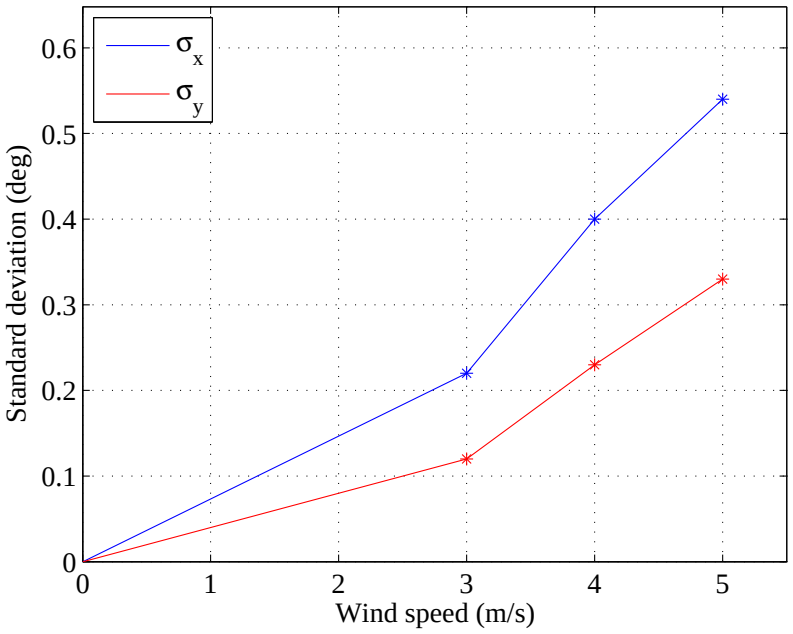

Figure 7.3: The standard deviation of the approximated probability density functions received from the simulations wind a fetch size of 35 km and a varying wind speed. The blue line shows the deviations of the light in the x-direction and the red shows the deviation in the y-direction.

As stated in Section 6.2.2, the same study was conducted twice but with the horizontal component of the laser direction perpendicular to the wind direction in the second case. The results are presented in Table 7.2 and Figure 7.4. As can be seen, the difference with the previous investigation is minimal.

Table 7.2: The parameters of the probability density functions for different wind speeds. The fetch size is 35 km for all simulations.

Wind speed (m/s)	$\bar{x}$ (deg)	$\bar{y}$ (deg)	σ_x (deg)	σ_y (deg)
3	0.00	-0.03	0.23	0.13
4	-0.01	-0.03	0.39	0.24
5	0.02	-0.04	0.54	0.34

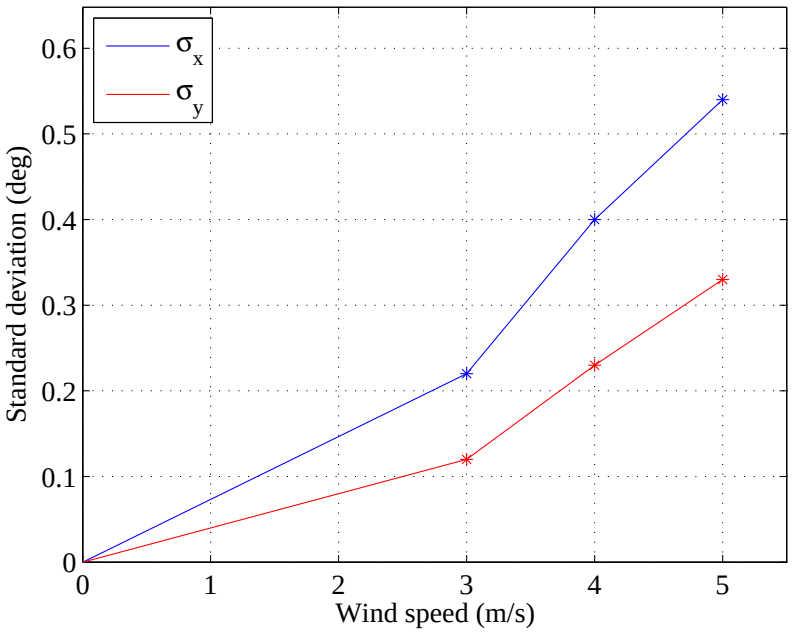

Figure 7.4: The standard deviation of the approximated probability density functions received from the simulations wind a fetch size of 35 km and a varying wind speed. The blue line shows the deviations of the light in the x′-direction and the red shows the deviation in the y′-direction.

The investigation of the fetch size dependence is shown in Table 7.3 and Figure 7.5. The sea is almost fully developed with a fetch size of 500 km with a wind speed of 3.5 m/s as could be seen earlier in Figure 4.1. This can also be

seen in the results in Figure 7.5 where the changes in direction deviation stops to increase for large fetch sizes.

Table 7.3: The parameters of the probability density function for different fetch sizes. The wind speed is 3.5 m/s for all simulations.

Fetch size (km)	$\bar{x}$ (deg)	$\bar{y}$ (deg)	σ_x (deg)	σ_y (deg)
10	-0.02	-0.00	0.17	0.10
25	-0.02	0.01	0.28	0.16
50	-0.05	0.0	0.35	0.20
100	-0.02	0.00	0.39	0.23
250	-0.00	0.00	0.43	0.25
500	-0.05	-0.01	0.44	0.26

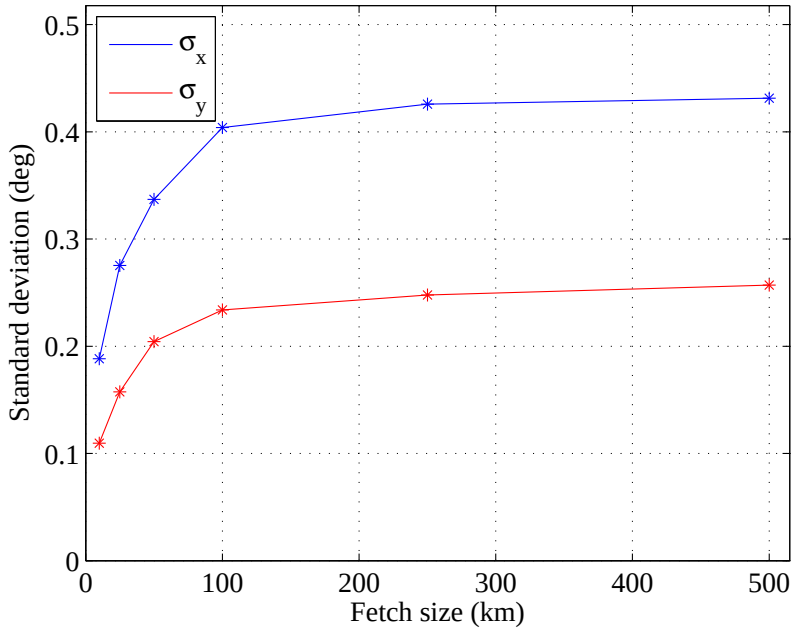

Figure 7.5: The standard deviation of the light direction of the approximated probability density functions received from the simulations with a wind speed of 3.5 m/s and a varying fetch size. The blue line shows the deviations of the light in the x′-direction and the red shows the deviation in the y′-direction.

The last investigation conducted was varying the size of the laser footprint on the water surface and the results are presented in Table 7.4 and Figure 7.6

Table 7.4: The parameters of the probability density function for different beam diameters. The fetch size is 10000 km and the wind speed is 5.4 m/s for all simulations.

Beam diameter (m)	$\bar{x}$ (deg)	$\bar{y}$ (deg)	σ_x (deg)	σ_y (deg)
0.0	-0.07	- 0.05	2.00	1.63
0.5	-0.09	0.02	1.49	1.06
1.5	-0.04	0.00	1.24	0.79
2.5	-0.05	0.03	1.05	0.64
3.5	-0.09	-0.02	0.90	0.56
4.5	-0.05	-0.01	0.84	0.49

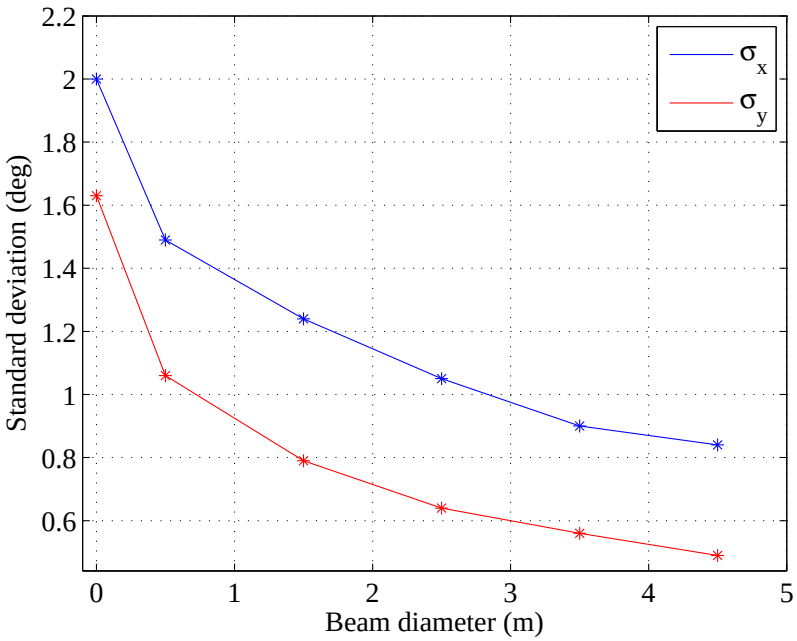

Figure 7.6: The standard deviation of the approximated probability density functions received from the simulations with a wind speed of 5.4 m/s, a fetch size of 10000 km giving a fully developed sea and

The deviations here are higher than in the previous cases since the wind speed was set to the maximum of 5.4 m/s and the fetch size is large enough for the sea to be fully developed.

7.1.1 Illumination ratio

The illumination ratio investigations use the same simulation data as the other theoretical investigations. Results obtained when analyzing the data from two simulations will be presented. The first one has a fetch size of 500 km and a wind speed of 3.5 m/s representing a nearly fully developed sea for this wind speed. In the second one, the fetch size has decreased to 10 km corresponding to a sea just starting to develop. The diameter of the laser footprint on the surface was 4.5 m in both simulations.

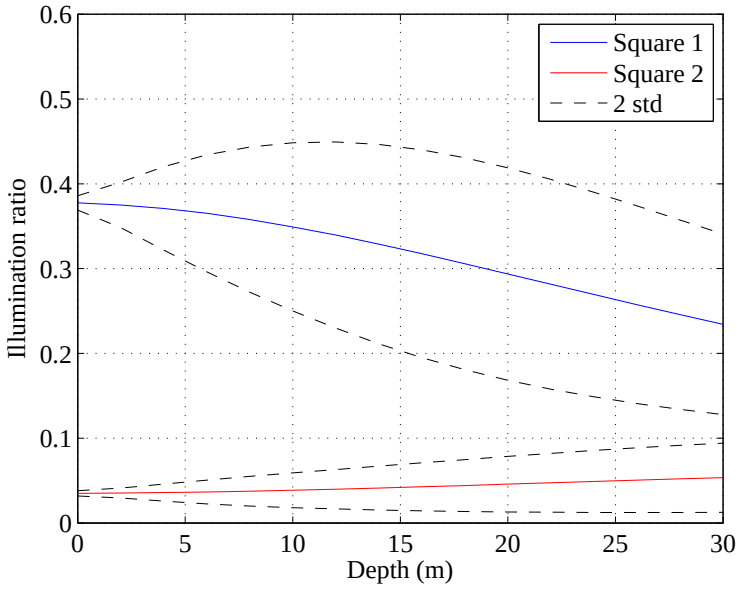

Figure 7.7: The illumination ratio of the two squares described in Section 6.2.6 as a function of depth. The wind speed was 3.5 m/s and the fetch size was 500 km. The dashed lines represent the limits of two times the standard deviation. 95 percent of the pulses are expected to fall inside those limits.

At a water depth of 15 m the standard deviation is 0.060 for square 1 and 0.014 for square 2 when the sea is almost fully developed. This can be seen in Figure 7.7. For the smaller fetch size, the standard deviation for square 1 is 0.05 and for square 2 0.01, at the same water depth as seen in Figure 7.8.

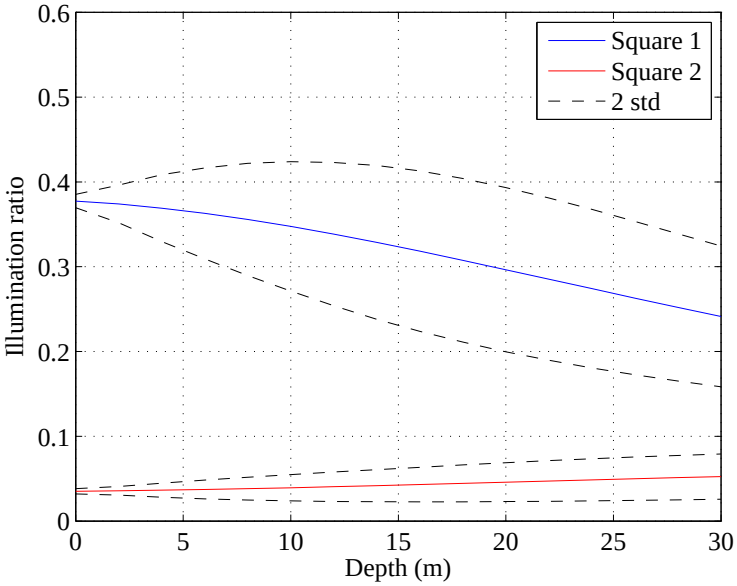

Figure 7.8: The same simulation as in Figure 7.7 but with a fetch size of 10 km.

7.2 Experiment results

The experiment results when all images are analyzed provides information similar to Figure 6.12 but were the coordinate system is expressed in length units describing the coordinates of the main intensity on the plastic sheet rather than angles. The Gaussian distribution parameters to a direction distribution are estimated according to Figure 7.9. The result has been adjusted with the reference value received when the directions for flat water were examined. Since the distance to the intersection point of the surface is known, a conversion to angles is easily done and presented in Table 7.5

Table 7.5: The estimated distribution parameters received from the measurements.

$\bar{x}$ (deg)	$\bar{y}$ (deg)	σ_x (deg)	σ_y (deg)
-0.20	0.08	0.76	0.37

The above values do not give any interesting information on their own but should be compared with the simulated results described in the next section. They should not be compared with real ocean simulation results because their method of analysis differ vastly.

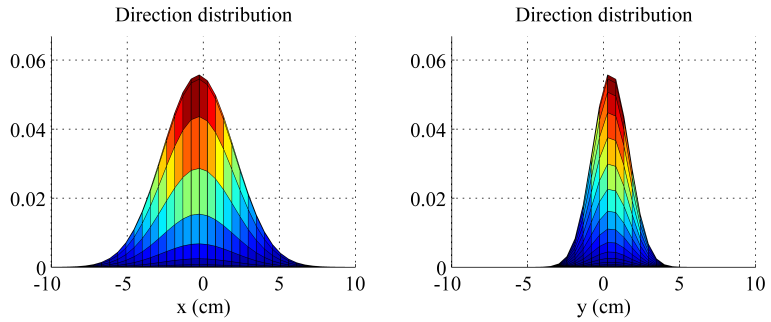

Figure 7.9: The approximated direction distribution seen from different points of view.

7.3 Wave tank simulations

As mentioned previously in Section 6.2.7, the analysis of the simulated photographs needs to be done in a similar way as for the real photographs. The threshold value, used for extracting the noise, is important for the end result. A low threshold will give smoother data and less variability. A too high threshold gives the opposite. Table 7.6 shows the simulation results for three different threshold values where the threshold is expressed as a ratio of the maximum pixel value. The threshold value in the real image analysis was around 65 percent.

Table 7.6: The estimated distribution parameters received from the wave tank simulation for different pixel threshold values.

Threshold	$\bar{x}$ (deg)	$\bar{y}$ (deg)	σ_x (deg)	σ_y (deg)
0.60	0.02	-0.12	0.64	0.32
0.65	0.00	-0.10	0.72	0.33
0.70	0.00	-0.08	0.74	0.36
0.75	-0.01	-0.13	0.77	0.41

7.4 Discussion and conclusions

The results from real ocean simulations show that the slope distribution of the ocean surface have a significant impact on how the beams deviate from the mean direction after the air/water interface. They also show that the picture of how it affects the directions is not trivial and very much depends on wind speed and fetch size. It is also shown that the size of the laser footprint is an important factor. However, none of the investigations show any significant change in the mean direction of the pulses. It appears that the flat water approximation

actually is a rather good estimation when considering the most likely angle of refraction to occur.

Increasing wind speeds yield increasing inaccuracy where the change appears to grow proportionally to the wind speed. It is important to note that in this investigation the sea is not fully developed and therefore the values do not correspond to the maximum deviation. The results of the two wind studies - where the only difference in set-up was the laser direction relative to the wind direction - shows no change. This will be discussed further, later in this section.

By studying the information in Figure 7.5 from the fetch investigation it is clearly seen that the changes are most significant when the sea is building up. The wind speed in this case was 3.5 m/s and higher wind speeds need larger fetch size to develop. However, it can be assumed that this yield similar shapes.

The size of the footprint has a significant impact. Figure 7.6 shows that small footprints are likely to deviate more than large ones. The reason for a larger footprint to be less affected is that the footprint is illuminating more facets giving an averaging effect. A small footprint does not illuminate as many facets and therefore the averaging effect is smaller. It is also an effect rising from the fact that a large footprint is less likely to strike a wave larger than the footprint. A small footprint intersecting the surface may strike the side of a wave causing the entire surface to appear tilted. The probability of a small footprint hitting a wave big enough for this effect to occur is obviously higher than for a larger footprint.

The ratio between the deviation in the y-direction respective the x-direction appears relatively constant around 0.5-0.6, when studying the impact of wind and fetch. This does not seem to be the case when the impact of the footprint size is studied. Instead, the ratio appears to increase with smaller footprints up to a maximum of 0.82.

When examining the results from the illumination ratio investigations, for the fully developed sea, it is clearly seen that the ratio decreases for square 1 with increasing water depth. It can also be seen that the deviation of the ratio increases with increasing water depth down to around 15 m and then remains fairly constant. At this depth, around 98 percent of the pulses are likely to have an illumination ratio at 20 percent or higher regarding square 1.

Studying the results for square 2 gives a different behavior. The illumination ratio increases slightly with increasing water depth due to the broadening of the pulse. However, the ratio remains low and at a water depth of 15 m only four percent of the light illuminates square 2 in average.

The effects are similar for the investigation using a fetch size of 10 km. When studying the average illumination ratio, and comparing with a larger fetch, it remains almost unchanged for both squares. The change is more clearly seen when studying the standard deviation. For square 1, the estimated illumination ratio is 0.2 or more for 98 percent of the surfaces at a water depth of 20 m.

It is important to point out that this study only takes into consideration the effect from the ocean surface. There are additional effects from the water column that will cause the results to differ from those in the simulations. The effects from the water column depend highly on the water quality and increase with increasing depth. Therefore, the present result should be used with care and considered more suitable for smaller depths than for larger ones. The water column adds scattering of the light, most likely yielding a lower illumination ratio than obtained from the present results. The water column has also a

smoothening effect on the light directions and it is reasonable to believe that deviations between pulses would become smaller than the estimates from this study. This topic has to be studied further, however, it is outside the scope of this study.

The investigation about the beam size also tells something about the maximum deviations, since the investigation used the top wind speed of 5.4 m/s and had a fetch size allowing the sea to be fully developed. The maximum standard deviation ranges from 0.84 degrees to 2.00 degrees. Guenther estimated the standard deviation of the horizontal error to be 0.36 m at a depth of 10 m and wind speeds of 5.4 m/s. This corresponds to a standard deviation of 2 degrees. Guenther does not mention for what beam size this estimation was done, but if it was for a very narrow beam a perfect agreement was found. If he used a broader beam this investigation gives a lower value of the deviation than his estimate.

One needs to remember that the results from the simulations are very dependent on the wave spectrum mode applied. If the model used is not able to represent the wave spectrum correctly, then that will directly affect the simulation results. A problem one has is that the majority of wave spectrum models focus on higher wind speeds than the ones of interest in this study. It is reasonable to assume that the agreement between the present model and reality becomes smaller when the wind speed decreases.

A solution to this would be to measure wave spectra directly on real ocean surfaces instead of using models. By gathering a set of measured wave spectra for different ocean conditions with focus on small wind speeds and then re-do exactly the same investigation as have been done here, the effect rising from the misbehavior in the wave spectrum models will be eliminated. Nevertheless, in this first stage of software development the use of models has been beneficial.

It is also important to remember that the Linear Wave Theory was consequently used in this study. Even though the theory is able to describe many aspects of the ocean, it does have limitations. When considering the large scale structure of the ocean surface this model works very well. However, for smaller waves - when surface tension becomes important - the linear theory becomes less accurate. Non-linear effects start to occur for those wavelengths, which the theory is not able to describe. From an optical point of view, small surface waves are important, and not being able to present them accurately is indeed a problem.

The validation of the method, where the results from the experimental measurements are compared with the simulated experimental results, shows good agreement. Especially the ratio between the deviation along the y'-direction and the x'-direction, where almost the same values were obtained in both investigations. This indicates that the angular spreading function was a good choice. The level of the threshold is a problem since it has an impact on the magnitude of the deviation. However, by choosing the same threshold value as when analyzing the real photographs one ends up with very similar results.

One thing that do differ between the two studies is the mean direction of all pulses along the x'-axis. The mean direction calculated from the photographs shows a shift towards the wind. This is a shift sideways, not seen in any other of the simulations. Most likely this is due to the effects one cannot simulate with the use of linear theory.

Nevertheless, the developed method provides a tool for making better esti-

mates of how the accuracy of a survey is affected by the environmental conditions at the survey site. The three main goals of the study were reached. The approximation of the ocean surface as flat - when estimating the average main refracted light direction - was justified for the examined environmental conditions. The variability of the main direction was quantified yielding insights about the accuracy due to the shape of the water surface for different environmental conditions. Finally, the confinement of the pulses and the illumination ratio of objects on the seafloor were successfully investigated and related to the surface conditions.

New wave spectrum models and wave measurement data can easily be implemented into the present model, developing the method further. Eliminating or having control of the error in all steps of the survey procedure is crucial and this study adds a new piece to the puzzle.

Appendix

The directional spectrum is described in the ECKV model by

$$S(k,\varphi) = \frac{1}{k^4}(B_l + B_h)\frac{1}{2\pi}(1 + \Delta k \cos(2\varphi)) \tag{7.1}$$

where k is the wavenumber, φ is the angle in comparison with the wind direction, B_l is the long-wave curvature spectrum, B_h is the short-wave curvature spectrum and Δk is the upwind-crosswind ratio.

The long-wave curvature spectrum is described by

$$B_l = 0.003\sqrt{\Omega} \cdot \sqrt{\frac{k_p}{k}} \cdot e^{-\frac{5k^2}{4k_p^2}} \cdot \gamma^{e^{-\frac{\left(\sqrt{\frac{k}{k_p}}-1\right)^2}{0.0128\left(1+\frac{4}{\Omega^3}\right)^2}}} \cdot e^{-\frac{\Omega}{\sqrt{10}}\left(\sqrt{\frac{k}{k_p}}-1\right)}$$

where

$$k_p = g\left(\frac{\Omega}{V_{10}}\right)^2$$

and

$$\Omega = \tanh\left(\left(\frac{g \cdot x}{22000 \cdot V_{10}}\right)^{0.4}\right)^{-0.75}$$

The short-wave curvature spectrum is described by

$$B_h = \frac{\alpha_m}{2} \cdot \sqrt{\frac{k_p}{k}} \cdot e^{-\frac{5k^2}{4k_p^2}} \cdot \gamma^{e^{-\frac{\left(\sqrt{\frac{k}{k_p}}-1\right)^2}{0.0128\left(1+\frac{4}{\Omega^3}\right)^2}}} \cdot e^{-\frac{1}{4}\left(\frac{k}{k_m}-1\right)^2}$$

where

$$\alpha_m = \begin{cases} 0.01\,(1 + \ln(u^*/c_m)) & \text{for } u^* < c_m \\ 0.01\,(1 + 3\ln(u^*/c_m)) & \text{for } c_m < u^* \end{cases} \tag{7.2}$$

and

$$u^* = 0.42\frac{V_{10}}{\ln(10/z_0)}, \qquad z_0 = 3.7 \cdot 10^{-5}\frac{V_{10}^2}{g} \cdot \left(\frac{V_{10}}{c_p}\right)^{0.9} \tag{7.3}$$

Δk is described by

$$\Delta k = \tanh\left(\frac{\ln(2)}{4} + 4\left(\frac{c}{c_p}\right)^{2.5} + a_m\left(\frac{c}{c_m}\right)^{-2.5}\right) \tag{7.4}$$

Bibliography

[1] IHO,*Status of Hydrographic Surveying and Nautical Charting Worldwide*, Publication C-55, 3rd (2004), Latest Update 27 September 2011

[2] G. C. Guenther, *"Airborne Lidar Bathymetry"*, in the DEM users manual, in Digital Elevation Model Technologies and Applications, Maune, D. F., Ed. Bethesda, MD: ASPRS, 2007, pp. 253-320.

[3] Airborne Hydrography AB, www.airbornehydrography.com, October 2011

[4] C. Cox and W. Munk, *Measurement of the Roughness of the Sea Surface from Photographs of the Sun's Glitter*, Journal of the Optical Society of America, vol 44, No 11, November1954

[5] Jerry Tessendorf, *Simulating Ocean Water*, 2005

[6] Robin Davidson-Arnott, *Introduction to Coastal Processes and Geomorphology*, Cambridge University Press, 2010

[7] T. Elfouhaily, B. Chapron, K. Katsaros, D. Vandemark, *A unified directional spectrum for long and short wind-driven waves*, Journal of Geophysical Research, Vol 102, No. C7, pp15,781-15,796, July 15 1997

[8] J. Wright, A. Cooling and d. Park, *Tides and Shallow-Water Processes*, The Open University, 1995

[9] Paul D. Komar, *Beach Processes and Sedimentation*, Prentice Hall, 1998

[10] Z. Demirbilek and C. Linwood Vincent, *Coastal engineering manual*, U.S. Army Corps of Engineers, USACE, 2002 engineer manual number: EM 1110-2-1100, Washington, DC, April, 2002.

[11] L.H. Holthuijsen, *Waves in Oceanic and Coastal Waters*, Cambridge University Press, 2007

[12] Harald E. Krogstad, Ovind A. Arntsen, *Linear Wave Theory - Part B*, Norwegian University of Science and Technology, 2000

[13] B.E.A. Saleh and M.C. Teich, *Fundamentals of Photonics,* 2^{nd}, Wiley, 2007

[14] O.M. Phillips, *The equilibrium range in the spectrum of wind-generated waves*, Journal of Fluid Mechanics, Vol 4, pp 426-434, 1958

[15] S.O. Rice, *Mathemathical Analysis of Random Noise*, Bell System Technical Journal, Vol 23, pp 282-332,1944

[16] W.H. Michel,*Sea Spectra Revisited*, Marine Technology, Vol 36, No. 4, pp 211-227, winter 1999

[17] C. B. Mobley, *Light and Water - Radiative Transfer in Natural Waters*, 2004

[18] G. A. Mastin, P. A. Watterberg, J. F. Mareda, *Fourier Synthesis of Ocean Scenes*, IEEE CG&A, March 1987, pp 16-23

[19] P. Frigaard, M. Hogedal, M. Christensen, *Wave generation theory*, Hydraulics&Coastal Engineering Laboratory, Department of Civil Engineering, Aalborg University, June 1993, p22

[20] NVIDIA, *CUFFT Library*, http://developer.download.nvidia.com /compute/ DevZone/docs/html/CUDALibraries/doc/ CUFFT_Library.pdf, September 2011

[21] IHO,*IHO Standards for Hydrographic Surveys*, Special Publication No. 44, 5th, February 2008

[22] MathWorks, http://www.mathworks.se/help/techdoc/ ref/filter2.html, October 2011